https://doi.org/10.5194/essd-2026-35
Preprint. Discussion started: 20 March 2026

# Transient snow line altitudes of glaciers in the European Alps from multi-mission remote sensing data (2000-2025)

Christian Sommer[1], Alexander R. Groos[1], Johannes J. Fürst[1], and Matthias Braun[1]

[1]Institute of Geography, Friedrich-Alexander-Universität Erlangen-Nürnberg, 91508 Erlangen, Germany

**Correspondence:** Christian Sommer (chris.sommer@fau.de)

**Abstract.** Observations of glacier snow line altitude (SLA) provide important information for estimating glacier surface mass balance and glaciological modelling. Optical satellite remote sensing enables the repeated measurement of SLA at glacier-specific to regional scales, yet producing continuous multi-temporal SLA time series requires the processing and analysis of large volumes of medium-resolution imagery. In addition, traditional image brightness thresholding may suffer from temporal changes in illumination, variations in reflectivity from evolving snow and ice surface properties, and cross-sensor radiometric differences. Here, we present a fully automated cloud-processing workflow for SLA retrieval based on optical image segmentation and adaptive, scene-specific thresholding, to map the snow-ice boundary on glaciers under various acquisition conditions and based on multi-mission data. Our method uses atmospherically corrected reflectance data from the Landsat-5 to -9 and Sentinel-2 satellite missions and accounts for cloud cover, non-glacier pixels, terrain shadows and temporal glacier surface elevation change. Our SLA dataset comprises a total of ∼200,000 observations across 408 glaciers in the European Alps between 2000 and 2025. In addition, we provide estimates of end-of-summer SLAs and multiannual change trends for most glaciers and years. Validation against visually delineated SLAs at selected reference glaciers demonstrates high agreement, with a root mean square error of ∼100 m vertical deviation. Applying the workflow to glaciers in the Alps reveals a mean regional SLA rise of 145 m since 2000 (+6 m year$^{-1}$), characterized by pronounced interannual variability. Particularly during the last decade, seasonal SLA change can be tracked due to the short revisit times of the current Landsat-8, -9 and Sentinel-2 earth observation missions. All data are publicly available at Zenodo (https://doi.org/10.5281/zenodo.18223929; Sommer et al. (2026)).

## 1 Introduction

Glaciers are a vital component of the hydrological cycle in mountainous and downstream regions (e.g. Immerzeel et al., 2020), providing meltwater runoff that regulates seasonal water levels in major streams (e.g. Huss, 2011), supports food security (e.g. Lutz et al., 2022), and produces hydroelectric power (e.g. Puspitarini et al., 2020). Moreover, glaciers and snow are considered Essential (Mountain) Climate Variables because they are critical for characterising the climate system and documenting changes in the (mountain) cryosphere in the context of global climate change (Thornton et al., 2021; GCOS, 2025). Observations of seasonal variations in snow cover extent and transient snow line altitudes (SLAs) - defined as the elevation of the transition between snow-free and snow-covered glacier ice at a given point in time - have long been used in glaciological studies to estimate annual variations in surface mass balance and meltwater runoff of mountain glaciers using satellite imagery (e.g.

Østrem, 1975; Williams et al., 1991; Turpin et al., 1997; Rabatel et al., 2005; Davaze et al., 2020). While multidecadal trends in End-of-Summer (EoS) SLA on alpine glaciers provide clear evidence of climatic changes in high mountain environments (e.g. Guo et al., 2021; Lorrey et al., 2022), high-resolution time series of snow-covered area fraction and SLA derived from remote sensing data are valuable for improving the representation of snow accumulation in glacier surface mass balance models (e.g. Barandun et al., 2018; Cremona et al., 2025).

In the context of global climate change, it has become essential to project the future evolution of glaciers under different emission scenarios to assess the impacts of ongoing glacier mass loss on global sea-level rise and runoff regimes in various mountain regions (e.g. Huss and Hock, 2018; Rounce et al., 2023). For this purpose, current regional and global glacier mass balance models (e.g. Rounce et al., 2023) are typically calibrated using available remote sensing products of glacier-specific ice mass changes for a given period obtained from spaceborne satellite data (e.g. Sommer et al., 2020; Hugonnet et al., 2021). However, calibrating multiple model parameters based on a single observation (e.g., geodetic mass change) often leads to model over-parameterisation and equifinality, meaning that multiple parameter combinations can produce similarly good agreement between modelled and observed glacier mass balance (e.g. Rounce et al., 2020; Schuster et al., 2023). This complicates the selection of suitable parameter sets and introduces ambiguity and uncertainty into long-term projections. Due to the relatively coarse temporal resolution (i.e., several years to decades) of satellite-derived geodetic mass change datasets, constraining glacier-specific mass balance gradients - and thus accumulation and ablation rates - remains challenging. Since different combinations of accumulation and ablation rates can counterbalance each other and still yield similar specific mass balances, poor calibration leads to large uncertainties in modelled mass balance gradients and future runoff projections (Schuster et al., 2023).

To address parameter equifinality and better constrain precipitation scaling/correction factors, which strongly influence modelled meltwater runoff, recent studies have incorporated additional observations (i.e., snow cover area fraction and SLA) into calibration strategies (e.g. Barandun et al., 2018, 2021). Incorporating SLA time series has been shown to improve modelled accumulation rates and sub-seasonal glacier mass balance by an average of 22 % and, in some cases, by up to 70 %, as demonstrated by Cremona et al. (2025). This highlights the considerable potential for integrating satellite-derived information on snow cover and snow line dynamics into glacier surface mass balance modelling. However, regional or global applications of this method remain limited, as consistent and long-term SLA time series are currently available only for individual glaciers (Barandun et al., 2018; Cremona et al., 2025) or selected mountain regions (Racoviteanu et al., 2019; Barandun et al., 2021; Loibl et al., 2025).

Optical imagery from different satellite missions is a suitable data source for creating long-term and glacier-specific SLA time series for entire mountain regions, owing to the high spatial coverage and repeated observations of glacier surface properties across mountain ranges over the past few decades. However, large-scale snow cover products based on satellite imagery, such as the Copernicus Fractional Snow Cover (EEA, 2025) and Theia Snow Collection (Gascoin et al., 2019), do not specifically distinguish between bare glacier ice and snow cover. Therefore, these datasets cannot be used to observe the seasonal evolution of SLA on individual glaciers. Detecting zones of bare ice and snow on glacier surfaces is challenging due to the large number of glacierised areas worldwide and the associated effort required to analyse large quantities of satellite imagery. More importantly, because of the relative similarity in spectral reflectance between snow-free and snow-covered glacier ice, "traditional" spectral band combinations for mapping snow and glacier areas, such as the Normalized Difference Snow Index (NDSI), are ineffective for classifying glacier snow cover. Conversely, near-infrared or infrared-to-shortwave-infrared ratios allow for a clearer separation between snow and ice, while experiencing less saturation over bright snow areas than visible channels (Hall et al., 1987; Matzl and Schneebeli, 2006). Consequently, previous assessments have either used visual detection of the SLA based on manually selected satellite images (Zhang and Kang, 2017; Larocca et al., 2024) or applied a single or set of constant reflectance threshold values to classify snow-covered pixels (Racoviteanu et al., 2019; Loibl et al., 2025). While manual delineation of SLAs is too time-consuming for decadal satellite image time series covering entire mountain ranges with extensive glacierized areas, surface classification using a fixed threshold can be affected by time-varying image illumination, such as changes in solar geometry and acquisition orbits (Zhang and Roy, 2016; Martín-Ortega et al., 2020). Additional uncertainties may arise from differences in the spectral bandwidths of remote sensing instruments (Chastain et al., 2019) or from glaciers being shaded by fractional cloud cover or nearby high mountain terrain (Rastner et al., 2019). Thus, depending on scene- and glacier-specific acquisition conditions, a fixed threshold value can result in either an underestimation or overestimation of snow cover extent (Paul et al., 2016).

To account for the time-varying reflectance properties of glacier surfaces, previous studies have presented adaptive reflectance thresholding methods that determine scene-specific threshold values using supervised classification (Pandey et al., 2013), machine learning (Prieur et al., 2022) or image segmentation (Rastner et al., 2019; Gaddam et al., 2022). In particular, Otsu's method (Otsu, 1979) has been adopted by recent studies (Rastner et al., 2019; Gaddam et al., 2022; Li et al., 2022; Ortiz Diaz et al., 2024) to classify glacier reflectance values into two distinct classes (snow and ice) by calculating the inter-class variance from image brightness histograms. As Otsu's method relies solely on the probability distribution of spectral reflectance across the glacier surface, without the need for empirically determined intensity thresholds, it is a promising approach for automatically mapping glacier snow cover and SLA under various conditions.

In this study, we present a fully automated, Otsu-based method for observing transient SLAs on glaciers in the Alps between 2000 and 2025. Our approach uses freely available global satellite imagery from the Landsat and Sentinel-2 missions. Snow cover classification on glaciers is implemented on the Google Earth Engine (GEE) geospatial data analysis platform, enabling snow cover extent and SLA to be assessed for individual glaciers and image acquisitions without the need to download and locally process large volumes of Earth observation data. To distinguish between snow and ice, we filter optical satellite images for cloud cover, terrain shadows and mixed pixels (e.g., debris at glacier margins) before applying a multi-channel mask based on Otsu thresholding. We employ the algorithm on band ratios of visible and infrared reflectance for each glacier and scene, thereby accounting for various snow facies and image acquisition conditions. The estimated snow cover masks are then converted into SLA values using a digital elevation model (DEM) and a vertical correction factor derived from rates of glacier surface elevation change (Hugonnet et al., 2021). The resulting dataset comprises 200,000 SLA observations distributed across 408 glaciers with an area of $\geq$1 km$^2$, corresponding to approximately 75 % of the total glacierized area of the Alps. Finally, we assess the vertical accuracy of the SLA algorithm by comparing the derived elevation values with manually delineated snow lines. To reveal spatial variations in SLA characteristics and quantify changes in the EoS SLA in response to global climate change, we calculate the multi-annual mean EoS SLA as well as long-term EoS SLA trends for all considered glaciers during the period 2000-2025.

## 2 Data

The processing workflow and data used in this study are based on the cloud-based Google Earth Engine (GEE) computing platform. GEE combines a repository of publicly available satellite remote sensing data ("Data Catalog") with a parallel processing system that automatically distributes computational tasks among a pool of high-performance servers (Gorelick et al., 2017). Access to data and analysis requests is provided via an application programming interface (API) or a web-based interactive development environment (IDE). The satellite image, surface elevation and glacier area data presented here were derived from the main GEE data archive and the "awesome-gee-community-catalog" repository (Samapriya et al., 2025).

### 2.1 Optical satellite images

We observe spatiotemporal glacier surface properties from changes in reflectance in infrared and visible light spectra. To analyse the seasonal to decadal extent of snow cover on glaciers in the European Alps, we use optical remote sensing image acquisitions from the Landsat-5, -7, -8, and -9, and Sentinel-2 satellite missions between January 1st, 2000 and October 20th, 2025. The Landsat mission is a long-term earth observation program of the National Aeronautics and Space Administration (NASA). Visible light and infrared reflection of the earth surface are acquired since the 1980s by the Landsat-5 Thematic Mapper (TM), Landsat-7 Enhanced Thematic Mapper Plus (ETM+) and Landsat-8 and -9 Operational Land Imager (OLI) imaging sensors at a spatial resolution of 30 m for the visible and infrared channels (Irons and Dwyer, 2010; Wulder et al., 2022). The repeat cycle between image acquisitions of each Landsat satellite is 16 days, but was reduced to 8 days due to the parallel operation of Landsat 5 and 7 and Landsat 8 and 9, respectively (Kaewmanee et al., 2023; Teillet et al., 2001). The Sentinel-2 mission of the European Space Agency (ESA) consists of two identical satellites, Sentinel-2A and Sentinel-2B, which are equipped with the multi-spectral instrument (MSI) providing a spatial resolution of 10 m in the visible and near-infrared and 20 m in the shortwave infrared spectra (Spoto et al., 2012). The Sentinel-2 MSI band designations are similar to those of the Landsat TM, ETM+ and OLI instruments, but cover a slightly narrower spectral bandwidth. The combined revisit time of Sentinel-2A and Sentinel-2B is 5 days (Drusch et al., 2012). The appendix provides an overview of the specific satellite mission operation periods, product specifications and the number of images available covering glaciers in the Alps (Table A1). In this study we employ the USGS Landsat 5-9 Level 2, Collection 2, Tier 1 (USGS, 2020) and Sentinel-2 MSI, Level-2A (ESA, 2021) products which have been converted from top-of-atmosphere (TOA) to orthorectified surface reflectance (bottom-of-atmosphere: BOA). The estimation of BOA reflectance is based on the Landsat Ecosystem Disturbance Adaptive Processing System Version 3.4.0 (LEDAPS) for Landsat 5 and 7 (Vermote and Saleous, 2007), the Land Surface Reflectance Code (LaSRC) for Landsat 8 and 9 (Vermote et al., 2018) and Sen2Cor for Sentinel-2 (Main-Knorn et al., 2017). The applied atmospheric corrections include the estimation of aerosol scattering, water vapor and thin clouds. Terrain corrections are performed using the surface topography of the global SRTM DEM, ASTER GDEM, Copernicus GLO-30 and other regional

DEMs (Franks et al., 2020; Gascon et al., 2017). It should be noted that the accuracy of topographic correction is related to the DEM data used (Dozier et al., 2022) and may vary between datasets and survey periods. However, we cannot assess a scene-specific uncertainty value for the conversion of TOA reflectance, since there are no systematic error assessments of the different correction algorithms and input data.

### 2.2 Glacier outline data

Outlines of glaciers in the Alps are provided by the Randolph Glacier Inventory (RGI) version 7.0 (RGI-7.0-Consortium, 2023). The RGI is a global collection of glacier areas, excluding the Antarctic and Greenland ice sheets, that approximately represents the extent of glacierized areas in 2000. Alpine glacier areas were extracted from the RGI region "Central Europe" and are based on thresholding of optical image band ratios and manual delineation (Paul et al., 2011). As the estimation of snow cover and SLA tends to be unreliable for very small glaciers due to the spatial resolution of optical satellite data, glaciers with an area of less than 1 km$^2$ were excluded from the subsequent analysis. Consequently, 408 glaciers with a cumulative area of $\sim$1600 km$^2$ were selected. This corresponds to 75 % of the total glacierized area of the European Alps. To reduce computational costs, particularly for masking large stacks of satellite image raster data, we simplified the selected glacier geometries by increasing the minimum distance between neighboring vertices along the polygon outlines to 60 m.

### 2.3 Glacier surface elevation data

The hypsometric distribution of snow cover and bare ice across the glacier surface is derived from digital surface elevation data. We use interferometric synthetic aperture radar (InSAR) data of the Shuttle Radar Topography Mission (SRTM) from the National Aeronautics and Space Administration (NASA) to extract the surface elevations of glaciers in the European Alps. The SRTM mission acquired C-Band SAR data of all land areas between 60°N and 56°S during the period 11-21 February 2000 (Farr et al., 2007). We use the void-filled SRTM NASADEM Merged DEM Global 1 Arc Second V001 (JPL, 2020) with a spatial resolution of 30 m. Compared to the previous SRTM V3, the more recent NASADEM has been reprocessed based on additional reference altimeter data from ICESat-1, as well as an improved phase unwrapping algorithm, resulting in a higher vertical accuracy and less void-filling (Crippen et al., 2016). To account for changes in glacier surface elevation since the NASADEM was acquired in 2000, we refer to maps of elevation change of the European Alps (Hugonnet et al., 2021). Rates of glacier surface elevation change are based on temporally interpolated time series of stereo-photogrammetric DEMs from the Advanced Spaceborne Thermal Emission and Reflection Radiometer (ASTER), through Gaussian process regressions. We use the 20-year elevation change product, which provides surface elevation change rates (meters per year) for Alpine glaciers between 2000 and 2019 with a spatial resolution of 100 m.

https://doi.org/10.5194/essd-2026-35
Preprint. Discussion started: 20 March 2026

# 3 Methods

## 3.1 Satellite image processing

Time series of optical image acquisitions of the Landsat and Sentinel-2 missions between January 1st 2000 and November 2025 are created by selecting all scene footprints overlapping with glacier areas of the RGI region "Central Europe". To filter satellite images with a high cloud probability, we remove acquisitions with a fractional cloud cover of more than 75 %. In addition, the annual selection of satellite images is roughly constrained to the glacier ablation period (April 1st to November 30th) to exclude images from months where glaciers are entirely covered by snow. Raw digital number (DN) values of the selected satellite images are converted to reflectance units by applying the respective scaling factors defined for each sensor (Chander et al., 2009). The image acquisition parameters, such as date and time, solar zenith and azimuth as well as acquiring sensor, are stored alongside each image. The image segmentation analysis is constrained to glacier areas by masking the optical images to the glacier outlines of the RGI. We use three optical band ratios of visible and infrared light to detect pixels which are either snow or ice and estimate the extent of snow cover and SLA based on the respective reflectance characteristics of the two surface classes. The surface types of pixels located within the RGI outlines are primarily snow and ice, depending on the image acquisition date and extent of snow melt, and mixed pixels, i.e. from supraglacial debris cover or fractional rock cover at the glacier margins. In infrared spectra, snow-covered areas appear bright due to their high reflectivity, while bare ice and rocks typically appear dark (Hall et al., 1987). Using Eq. 1, we calculate the ratio ($NSIR$) of near-infrared ($NIR$) and short-wave infrared ($SWIR$), which improves the spectral separation between snow and ice compared to using the NIR band alone (Li et al., 2022).

$$NSIR = NIR\frac{NIR}{SWIR} \tag{1}$$

The high spectral reflectance of snow is related to the scattering of incoming radiation, which is controlled by grain size and the presence of air bubbles. In contrast, glacier ice is more compressed, resulting in a higher absorption rate and lower reflectance (Warren, 2019). Similarly, rocks and debris-covered ice absorb infrared, resulting in low reflectance (Shukla et al., 2009). These differences in brightness are beneficial for the detection of snow-covered pixels because ice and debris appear similarly dark, whereas snow can be easily distinguished. The Normalized Difference Water Index ($NDWI$), which is based on the $GREEN$ and ($NIR$) bands (Eq. 2), is an additional parameter used to estimate the presence of surface melt:

$$NDWI = \frac{(GREEN - NIR)}{(GREEN + NIR)} \tag{2}$$

The NDWI is also sensitive to wet snow and ice (Korzeniowska et al., 2017; Mizuochi et al., 2024) because the reflectance of both water and snow decreases similarly from the visible to the infrared spectrum. In particular, the low NIR reflectance of bare ice in areas where the glacier surface has partially melted results in high NDWI values compared to the upper, snow-covered accumulation area, and vice versa. Finally, the Normalized Difference Snow Index ($NDSI$) is calculated from the $GREEN$ and $SWIR$ bands following Eq. 3:

$$NDSI = \frac{(GREEN - SWIR)}{(GREEN + SWIR)} \tag{3}$$

The $NDSI$ is used to exclude cloud covered pixels (Choi, 2004) from the subsequent image segmentation. Snow and clouds both exhibit relatively high reflectivity in the Green band, but the reflectance of snow decreases in the $SWIR$ band while the reflectance of clouds remains high (Hall et al., 1995). The created band ratios are then stored as multi-channel images. To avoid the fragmentation of large, continuous glacier areas, for example due to glaciers located at the margin between image footprints, the band ratio images are merged based on their acquisition date, location and imaging sensor. Thereby, an image mosaic is created for each band ratio and for all images acquired by the same sensor on the same day. Ultimately, the daily image mosaics from each sensor are aggregated within a combined time series and sorted by the acquisition date.

### 3.2 Image filtering and segmentation

To accurately estimate the Otsu threshold between snow-covered and bare-ice zones, areas covered by clouds, as well as brightness values from mixed pixels containing rocks, snow and ice, such as at the glacier margins, must be removed beforehand. We follow previous studies that used the NDSI to remove clouds over snow-covered areas (Choi, 2004; Salomonson and Appel, 2004). A fixed NDSI threshold of 0.7 is used to select pixels belonging to the surface classes of snow or ice. The NDSI band of each image mosaic is then reclassified accordingly as a binary mask and applied to the NSIR and NDWI bands.

In addition to masking pixels containing clouds or rocks, we exclude pixels susceptible to shading by the surrounding terrain, as this can bias the classification by altering the local reflectance of the glacier surface (Paul et al., 2016). We use a geometric model based on satellite viewing geometry, surface topography and solar illumination at the image acquisition time, as defined by the solar zenith and azimuth angles, to assess the presence of terrain shadows. Pixels are classified as shaded when the maximum terrain elevation angle towards the sun exceeds the solar elevation angle (Corripio, 2003). As estimating image-specific terrain shading is computationally expensive for large time series, we calculate a binary terrain shadow mask every 10 degrees between the minimum and maximum sun azimuths, mean sun elevation, and surface elevations of the NASADEM. The shadow masks are then merged to exclude pixels likely to be shaded by terrain in most images.

For the subsequent discrimination of snow and ice pixels, we use Otsu's method of automatic image segmentation following previous studies (Gaddam et al., 2022; Li et al., 2022; Rastner et al., 2019; Yin et al., 2013). Otsu's method is an unsupervised image segmentation technique that identifies two homogeneous image intensity classes, which are separated by a threshold value. Therefore, Otsu's method is based on the assumption that an input image can be represented as a bimodal histogram with two distinct peaks, for example, the different brightness of glacier areas covered in snow or bare ice. The optimal threshold value between these two classes is then calculated by maximizing the inter-class variance, or equivalently minimizing the intra-class variance (Otsu, 1979). As the Otsu threshold is histogram based, extremely low or high reflectance values, such as low NIR reflectance of ice impurities or saturation of SWIR over bright accumulation areas, could result in varying bin intervals.

Therefore, we select all late-summer images (August-September) where the presence of a bimodal surface class distribution (i.e. bare ice and snow) is very likely and calculate for each pixel the minimum and maximum brightness value in the NSIR band over the 25 years observation period. The valid range of snow and ice reflectance values for the NSIR band is then estimated as the 10 % and 90 % percentiles of the observed minimum and maximum reflectance, respectively. Thereafter, Otsu's method is applied for the NSIR reflectance of each glacier. For each glacier and date, the output comprises the Otsu threshold and a corresponding binary mask (Fig. 1).

For a small number of late-summer images we observe a sharp increase in NSIR reflectance at low elevations. This causes a detection of seamingly snow cover of the ablation area while the visible spectra bands indicate bare ice across the glacier. We attribute this effect to refreezing processes of the glacier surface which increase the NIR reflectance (Florath et al., 2022). To avoid a false detection of snow, we therefore use the NDWI band to reject pixels with an NDWI value >0.1, which typically indicates wet ice or water (Dell et al., 2022). The final glacier-specific snow cover is then derived from intersecting the Otsu-masked NSIR and 0.1 threshold-masked NDWI bands (Eq. 4):

$$\mathrm{SNOW}(x) = \big(\mathrm{NDSI}(x) \geq 0.7\big) \,\wedge\, \big(\mathrm{NSIR}(x) \geq T_{\mathrm{Otsu}}\big) \,\wedge\, \big(\mathrm{NDWI}(x) \leq 0.1\big). \tag{4}$$

where $\mathrm{SNOW}(x)$ are the pixels of an image $(x)$ detected as snow and $T_{\mathrm{Otsu}}$ is the Otsu-derived threshold computed from the NSIR histogram. Thereby, the fixed NDSI threshold of 0.7 is applied prior to the Otsu segmentation to exclude pixels which are neither snow or ice. Thereafter, the remaining glacier surface is classified into snow and ice based on the automatic reflectance separation of the NSIR reflectance. Finally, a fixed NDWI threshold of 0.1 is applied to remove misdetected pixels from the output snow mask.

### 3.3 Snow line altitude mapping

To derive the SLA, we aggregate the surface elevations of the NASADEM within 10 m elevation bins. The binned surface elevation values of the NASADEM are then extracted for each glacier and date, based on the respective binary Otsu snow mask. The SLA is usually not a continuous line that separates areas of snow cover and bare ice, but rather a transition zone that is characterized by patches of snow across the melting glacier surface. The lowest elevation of snow cover does not necessarily equate to the SLA, but refers to small clusters of snow from avalanches at the glacier margins or areas with thicker snow deposition. The SLA is therefore calculated as the 10th percentile of the snow-masked, binned DEM elevations. Notably, the NASADEM represents glacier surface elevations in February 2000. While this aligns well with the start of the SLA observation period on January 1st 2000, it is likely that there is an increasing vertical offset in the estimated SLA due to substantial glacier mass loss and surface lowering in the European Alps since 2000 (The GlaMBIE Team et al., 2025). Assuming a constant glacier surface elevation would introduce biases when extracting SLA long-term trends, depending on the glacier-specific melt rates during the 25-year observation period. To account for time-varying changes in SLA due to glacier surface lowering, we calculate an elevation correction factor for each SLA observation using maps of glacier surface elevation change between 2000 and 2019 (Hugonnet et al., 2021). Therefore, we extract the mean surface elevation change rate at the SLA elevation bin and

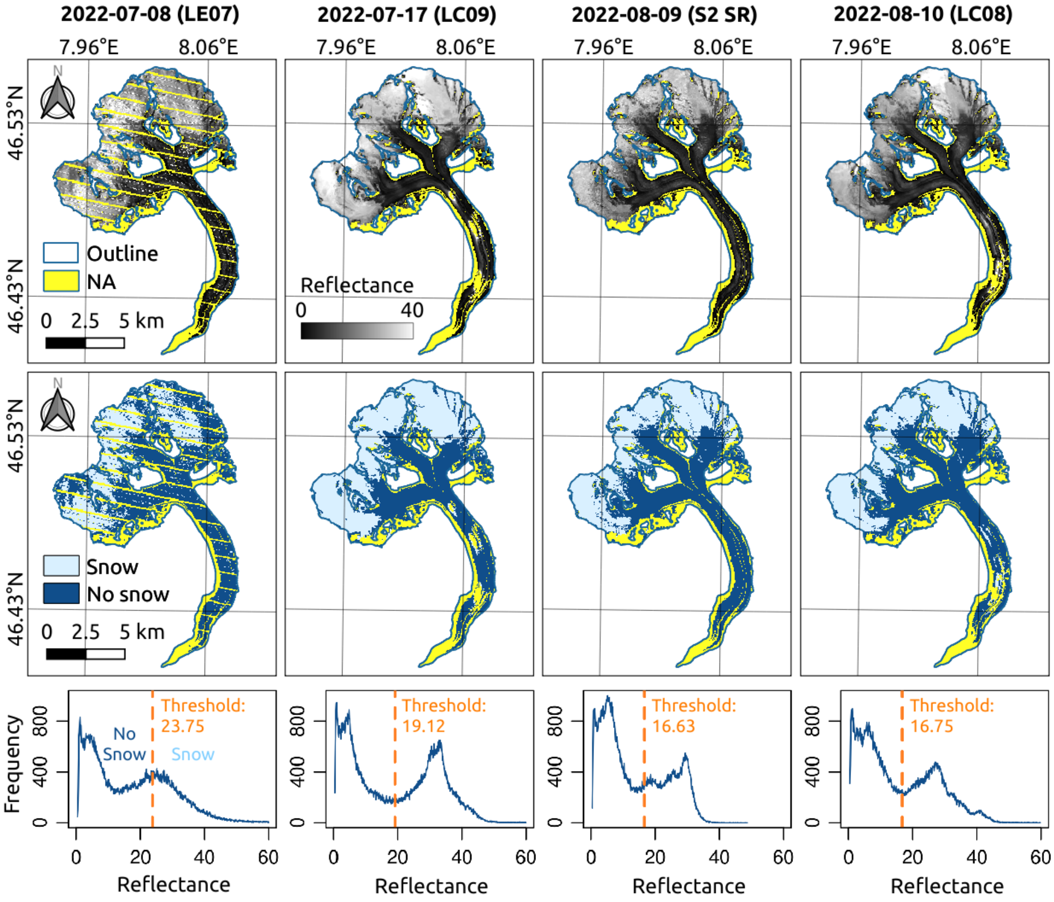

**Figure 1.** Image segmentation and snow cover mapping based on the near-infrared to short-wave infrared ratio (NSIR) for the spectral separation of snow and ice areas, illustrated for the Grosser Aletschgletscher: Spatial variations in the glacier's surface reflectance during the ablation season in 2022 derived from multi-mission satellite imagery (top row), with the corresponding binary snow cover maps (middle row) created using individual Otsu thresholding (bottom row).

determine the date difference between the NASADEM mean acquisition date (2000-02-16) and the acquisition date of the satellite image from which the SLA was derived. The total elevation correction factor is estimated by multiplying the mean surface elevation change rate (in meters per year) by the time difference.

As a final step of the SLA mapping, unreliable observations are filtered to reduce biased SLA estimates caused by undetected cloud artefacts or acquisition dates on which the glacier is entirely snow covered. Observations with very low spatial coverage are first screened, and SLA measurements based on images with less than 10 % coverage of the glacier area are rejected. This relatively low threshold is chosen because, depending on the spatial distribution of valid reflectance measurements, observations with limited coverage may still provide a meaningful SLA estimate. For the remaining observations, confidence levels are assigned based on a set of spatial and spectral filter criteria:

- Valid global coverage: Covering a relatively large fraction of the glacier surface (> 50 %) increases the probability of capturing the bimodal surface distribution of snow and ice pixels.

- Valid global area: Estimating the Otsu-based snow–ice threshold from a small area of valid pixels (< 0.5 km$^2$) increases the likelihood of erroneous SLA detection due to outliers or an uneven spatial distribution of reflectance values across the glacier.

- Valid snow-class area: Similar to the global area criterion, a small area of valid snow pixels increases the risk of misclassification. We apply a minimum snow-class area threshold of 0.09 km$^2$ which roughly corresponds to 100 pixels at 30 m spatial posting.

- NSIR standard deviation: A low standard deviation (SD) in the NSIR band indicates a highly homogeneous reflectance across the glacier, which often corresponds to complete cloud cover or complete snow cover. To ensure the presence of a bimodal reflectance distribution, the 10th percentile of all SD values (SD > 3) is used as a lower bound.

- NSIR Otsu threshold: Low Otsu thresholds may reflect non-snow surface types or cloud-contaminated reflectance values. The 10th percentile of all Otsu thresholds (Otsu = 7) is therefore applied as a lower bound for a meaningful discrimination between snow and ice.

- NSIR intra-class distance: In cases where glacier reflectance follows a unimodal distribution, the Otsu thresholding of the NSIR band may not be meaningful. To identify such cases, the Bhattacharyya distance between the probability distributions of ice and snow classes is calculated. Distance values close to zero indicate nearly identical distributions and thus unreliable classifications. Observations with distances $\leq 0.2$ are flagged accordingly.

Based on the combined outcome of these criteria, a confidence level is assigned to each SLA observation and appended as a quality flag (QA-FLAG) ranging from 0 to 1. Values close to 1 indicate observations that satisfy most or all filter criteria, whereas lower values denote SLA measurements with low spatial coverage or potentially unimodal reflectance distribution.

https://doi.org/10.5194/essd-2026-35
Preprint. Discussion started: 20 March 2026

### 3.4 Comparison of retrieved snow lines

To assess the accuracy of the automated SLA retrieval, Otsu-based SLA estimates are compared against independently derived reference snow lines, equilibrium line altitudes (ELA) and across individual satellite sensors.

Reference glacier snow lines are obtained by manual delineation using Sentinel-2 Level-1C true-color (RGB) imagery and the line drawing tool available in the ESA Copernicus Browser (https://browser.dataspace.copernicus.eu/). For manual mapping, only scenes with less than 50 % cloud cover and a visually distinguishable bare ice and snow zone are selected. To capture a broad range of glacier and snow cover conditions, glaciers and acquisition dates are chosen to represent different glacier morphologies, including debris-covered and clean-ice glaciers, as well as varying degrees of surface melt, reflected by low and high SLAs. In total, 890 reference SLAs were manually digitized for the period 2015–2025 across 23 glaciers (Table A2). Surface elevations of the manually delineated snow lines are estimated by generating a 100 m buffer around each line segment and intersecting the buffered geometry with the NASADEM. Then, the same temporal elevation change correction applied in the automated SLA processing chain is also used for the manually derived snow lines. Automated and manually derived snow line elevations are then compared by computing elevation differences for pairs of observations with a maximum acquisition time offset of five days.

In addition, we compare late summer SLA estimates with annual ELA values from surface mass balance data provided by the World Glacier Monitoring Service (WGMS) Fluctuations of Glaciers (FoG) Database (WGMS, 2025). Between 2000 and 2025, annual ELA values are available for 22 glaciers with an area of at least 1 km$^2$.

Finally, we assess the vertical deviation between snow lines extracted from images of different satellites by selecting SLA estimates from the same day or one day apart. Thereafter, we compute the pairwise differences for each sensor combination and calculate the mean deviation and root mean square error (RMSE).

### 3.5 Uncertainty analysis and error budget

To quantify the uncertainty of the Otsu-based reflectance thresholding and the resulting SLA estimates, the following error terms are considered:

- Error from limited spatial coverage of optical imagery ($\delta^{\mathrm{AREA}}_{\mathrm{covered}}$)
- Error from incomplete masking of clouds or other non-glacier surfaces by the NDSI-based mask ($\delta^{\mathrm{MASK}}_{\mathrm{glacier}}$)
- Error from reflectance outliers, such as extreme bright values ($\delta^{\mathrm{MASK}}_{\mathrm{extreme}}$)
- Error from pixels affected by terrain-induced shadows ($\delta^{\mathrm{MASK}}_{\mathrm{t.shadow}}$)
- Error the DEM-differencing elevation change correction ($\delta^{\mathrm{DHDT}}_{\mathrm{DEM\text{-}diff.}}$)

The total uncertainty ($\delta_{\mathrm{SLA}}$) of each SLA estimate is computed by assuming that individual error contributions are independent and combining them through quadratic error propagation (Eq. 5):

$$\delta_{\mathrm{SLA}} = \sqrt{\delta^{\mathrm{AREA}\,2}_{\mathrm{coverage}} + \delta^{\mathrm{MASK}\,2}_{\mathrm{glacier}} + \delta^{\mathrm{MASK}\,2}_{\mathrm{extreme}} + \delta^{\mathrm{MASK}\,2}_{\mathrm{t.shadow}} + \delta^{\mathrm{DHDT}\,2}_{\mathrm{DEM-diff.}}} \tag{5}$$

Limited spatial coverage, incomplete removal of clouds or other non-glacier pixels, the presence of reflectance outliers, and terrain shading can bias the NSIR histograms used for Otsu thresholding. Such biases may lead to either an under- or overestimation of the derived SLA. To quantify the individual uncertainty contributions of $\delta^{\mathrm{AREA}}_{\mathrm{covered}}$, $\delta^{\mathrm{MASK}}_{\mathrm{glacier}}$, $\delta^{\mathrm{MASK}}_{\mathrm{extreme}}$, and $\delta^{\mathrm{MASK}}_{\mathrm{t.shadow}}$, sensitivity experiments are conducted. In these experiments, SLAs derived by deactivating the respective filter algorithm are compared against SLAs obtained with all filters enabled. To simulate the effect of limited spatial coverage ($\delta^{\mathrm{AREA}}_{\mathrm{covered}}$), each glacier and acquisition date is artificially masked by generating a random number of points (10–100) across the glacier surface, which are subsequently buffered with widths ranging from 30 to 300 m to mimic missing observations. The resulting vertical SLA deviations are found to depend on the fraction of the glacier area covered by valid pixels (Fig. A1). Decreasing spatial coverage leads to increasing SLA offsets, as sparse and uneven sampling reduces the ability to accurately resolve the bimodal reflectance distribution and thus biases the Otsu-based separation. Accordingly, a linear relationship is applied that assigns larger uncertainty contributions to SLA estimates derived from scenes with lower spatial coverage. Incomplete non-glacier pixel masking, reflectance outliers, and terrain shadow masking ($\delta^{\mathrm{MASK}}_{\mathrm{glacier}}$, $\delta^{\mathrm{MASK}}_{\mathrm{extreme}}$, and $\delta^{\mathrm{MASK}}_{\mathrm{t.shadow}}$) may further affect the inter-class variance of ice and snow reflectance. Because the probability of biased reflectance values cannot be quantified for individual glaciers and acquisition dates, we use bulk uncertainty estimates. These are derived from the root mean square error (RMSE) of SLA deviations obtained from the respective sensitivity runs and amount to 88.0 m, 41.7 m, and 37.9 m for $\delta^{\mathrm{MASK}}_{\mathrm{glacier}}$, $\delta^{\mathrm{MASK}}_{\mathrm{extreme}}$, and $\delta^{\mathrm{MASK}}_{\mathrm{t.shadow}}$, respectively. Uncertainty associated with the glacier elevation change correction ($\delta^{\mathrm{DHDT}}_{\mathrm{DEM\text{-}diff.}}$) is estimated using the mean regional elevation change rate uncertainty of glaciers in the Alps (0.21 m $\mathrm{year}^{-1}$) as reported by (Hugonnet et al., 2021) multiplied by the time difference between January 1st 2000 and the acquisition date of the SLA estimate. As the elevation change maps only cover the period 2000-2019, we additionally multiply $\delta^{\mathrm{DHDT}}_{\mathrm{DEM\text{-}diff.}}$ by a factor of 2 for SLA estimates acquired after 2019-12-31.

### 3.6 Statistical analysis of the EoS SLA

To derive glacier-specific EoS SLA time series for 2000–2025, we identified the highest SLA observed on each glacier during the mid- to late ablation season, defined here as the period from 15 July to 30 September. When fewer than three suitable satellite scenes were available within this window, the corresponding annual EoS SLA estimate was subjected to an outlier-detection procedure. For glaciers with at least ten years of robust EoS SLA estimates (i.e. years with three or more valid scenes), a statistical filter was applied: EoS SLA values deviating by more than ±2 standard deviations from the glacier-specific multiannual mean were classified as outliers. For glaciers with fewer than ten such years, a physical threshold criterion was used instead, flagging any EoS SLA differing by more than ±400 m from the mean glacier elevation (derived from RGI) as an outlier. The mean EoS SLA for 2000-2025 was then calculated from all valid (i.e. non-flagged) years. These glacier-specific mean EoS SLAs were compared with six variables derived from the RGI (central longitude, central latitude, area, mean elevation, mean slope, and mean aspect) to assess the influence of glacier location, size, and geometry on the long-term mean EoS SLA.

EoS SLA trends for 2000-2025 were computed using linear regression for all glaciers that fulfilled the following three criteria: (i) at least 50 % valid EoS SLA observations within the study period ($n \geq 13$ of 26 years), (ii) a time series spanning at least 15 years, and (iii) at least one valid EoS SLA observation in at least four of the five 5-year blocks (2000-2004, 2005-2009, 2010-2014, 2015-2019, 2020-2024). Trend significance ($p$-value) was assessed using the $t$-test on the regression slope. To estimate the mean regional change in EoS SLA across the Alps, we first calculated the average of all glacier-specific trends. As an alternative approach, we also computed the relative EoS SLA deviation from the long-term mean (2000–2025) for each glacier and year with observations, derived the region-wide annual mean anomaly (ΔEoS SLA), and then estimated the long-term trend from this aggregated series.

The mean EoS SLA and the respective trends for the period 2000–2025 were calculated for 405 of the 408 considered glaciers. Three glaciers were discarded because no suitable observations were available during the mid- to late ablation season for the EoS SLA computation. To facilitate the use of the EoS SLA datasets, we created two summary tables (see Section 7): one contains the annual EoS SLA time series for each individual glacier ($n$ = 408), and the other represents an updated version of the RGI (version 7.0) with EoS SLA information for 405 glaciers. The following four columns were added to the updated RGI: (i) mean glacier-specific EoS SLA, (ii) number of years for which the EoS SLA could be calculated, (iii) EoS SLA trend, and (iv) trend significance ($p$-value).

## 4 Results

### 4.1 Snow line measurement frequency and accuracy

Applying the Otsu-based snow line retrieval workflow resulted in a total of  120,000 Landsat-5-9 and  103,000 Sentinel-2 SLA measurements (QA flag >= 0.75) derived from more than 13,000 satellite images. The temporal density of SLA observations varies throughout the study period (Fig. 2), primarily due to changes in satellite acquisition availability. Prior to the launch of Landsat 8 in 2013, the temporal sampling was limited by the relatively low acquisition frequency of Landsat 5 and 7, resulting in an average of less than 10 valid SLA measurements per glacier and year. Consequently, the first half of the time series contains significantly fewer observations. In contrast, temporal coverage improved after 2013 (> 10 SLAs per glacier and year) and in particular after 2017 with the operational availability of Sentinel-2 Level-2A products (approx. 40-50 SLA measurements per glacier and year). In combination with Landsat 8 and 9, this results in revisit intervals of a few days.

The impact of different reflectance filters on SLA accuracy is illustrated in Fig. 3(a-d). Removing specific reflectance filtering of non-glacier pixels, outliers, and terrain shadows (Fig. 3a–c) produces vertical offsets in the order of several tens of metres (RMSE ≈ 40-90 m) but does not substantially affect the correlation between filtered and non-filtered estimates ($r^2 > 0.91$). In contrast, larger discrepancies are observed for SLAs derived from scenes with reduced spatial coverage of valid glacier pixels (Fig. 3d). Here, the vertical offset increases to a RMSE of 162.6 m ($r^2 = 0.68$), indicating that spatially incomplete image data

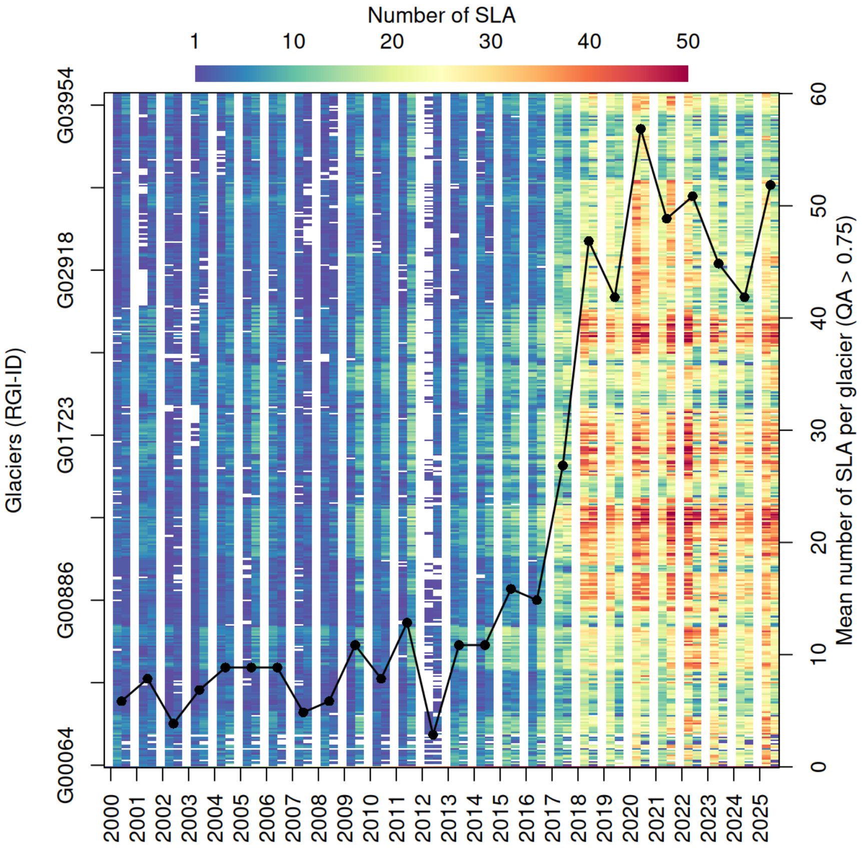

**Figure 2.** Number of suitable optical satellite images per year and sub-period (April to July and August to November) for SLA calculation on all glaciers considered across the Alps (n = 408) from 2000 to 2025. No scenes were processed for the winter period (December to March; white columns).

substantially reduces the accuracy of the histogram-based snow and ice separation. The mean uncertainty ($\delta_{\mathrm{SLA}}$) of all SLA measurements and SLAs based on images with a spatial coverage of more than 50 % is 127.4 m and 105.5 m, respectively.

The comparison between automated and manually delineated SLAs at the 23 selected test glaciers (Fig. 3e) shows a good agreement ($r^2 = 0.88$), with an absolute vertical deviation of approximately 100 m (RMSE = 95.7 m). Remaining discrepancies primarily occur under surface conditions where the transition between snow and bare ice is indistinct. Such conditions are primarily observed at the beginning and end of the glacier ablation period. Early in the melt period, snow thinning at the glacier terminus and the emergence of bare ice patches tend to cause an overestimation of the automated SLA. Conversely, widespread melt in late summer in the upper accumulation area, combined with isolated snow remnants along glacier margins or within shaded depressions, often results in an underestimation of the automatically derived SLA. Finally, the cross-sensor intercomparison of SLAs acquired within <1 days of one another reveals no systematic differences between image acquisitions

https://doi.org/10.5194/essd-2026-35
Preprint. Discussion started: 20 March 2026

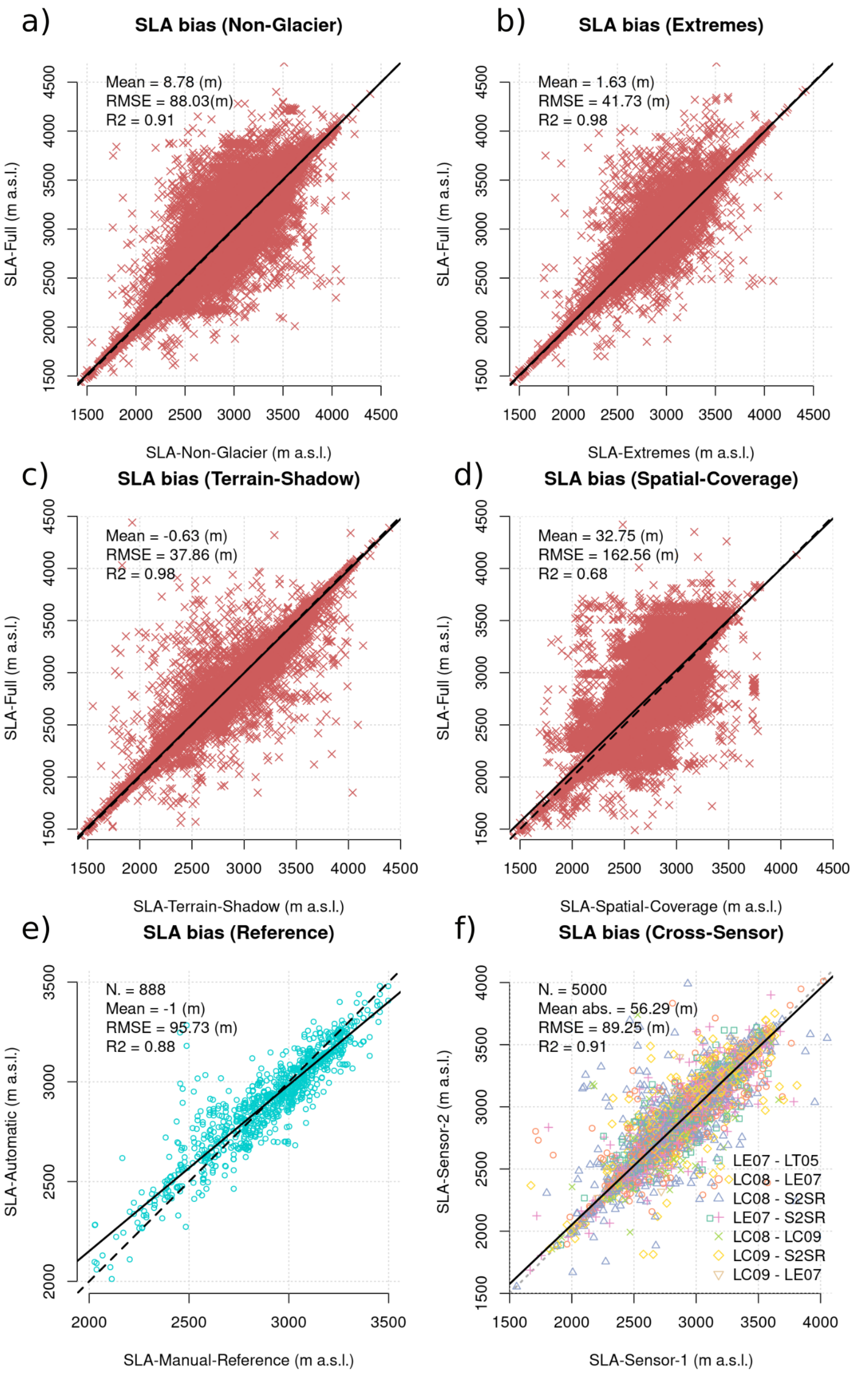

**Figure 3.** Overview of SLA uncertainty assessment: a) SLA offsets caused by not excluding pixels which are neither snow or ice; b) SLA offsets caused by no outlier filtering; c) SLA offsets caused by no masking of terrain shadows; d) SLA offsets caused by low spatial coverage of the glacier surface; e) Pairwise vertical difference between manually and automatically delineated SLAs at reference glaciers; f) Pairwise vertical difference between contemporaneous SLA estimates of different sensors (random sample of 5000 pairs).

of the individual optical satellite missions (Fig. 3f). The sensor-specific analysis shows a correlation of $r^2 = 0.91$ and a mean RMSE of 89.7 m, comparable to the deviation observed between manual and automated SLE measurements. Further detailed statistics on the comparison of glacier-specific offsets between manual and automatic SLAs and each sensor pair are provided in Table A2 and Table A3, respectively.

Fig. A2 shows the comparison between EoS SLAs and annual ELAs of individual glaciers. For ELAs below 3,200 m a.s.l., the EoS SLA and ELA are relatively similar, with ELAs tending to be located higher up the glacier than the corresponding EoS SLA estimate. Above 3,200 m a.s.l., much higher offsets can be observed, with some EoS SLAs being located hundreds of meters below the ELA. Therefore, the statistical deviation (RMSE = 212.9 m) is greater than the offset between automated and manually delineated SLAs.

## 4.2 Glacier-specific SLA variations and trends

Based on all suitable post-processed optical satellite images (QA flag = 1), transient SLA time series for the ablation season were derived for 408 glaciers across the Alps. Observation density, however, differs markedly between years due to satellite data availability. Years with an exceptionally high number of overcast days (e.g. 2002 and 2012) further exhibit a generally reduced number of SLA observations (Figs. 2 and 4). Individual glacier time series, such as that of Grosser Aletschgletscher, show the characteristic rise of the transient SLA during the ablation season and its abrupt lowering with the onset of snowfall at the beginning of the accumulation season (Fig. 4). The observations also reveal pronounced interannual variability in both the timing of SLA rise and the maximum SLA towards the end of the ablation season (cf. 2021 vs. 2022 and 2023 in Fig. 4b), and they capture individual summer snowfall events (see the SLA drop in 2024 in Fig. 4c).

For 98.5 % (n = 399) of the 408 glaciers, the EoS SLA could be determined for at least ten years, for 95.3 % (n = 386) for at least twenty years, and for 19.0 % (n = 77) for the entire period 2000-2025. The mean EoS SLA across all glaciers and years is 3039 ± 219 m a.s.l. Clear spatial patterns emerge (Fig. 5): relatively low EoS SLAs occur, among others, in the Bernese and Glarus Alps north of the Rhone, Reuss and Rhine valleys, and in the Silvretta and Tauern Alps. Intermediate values are found in the Bernina Range and the Ötztal Alps, while very high EoS SLAs up to ∼3600 m a.s.l. are observed on glaciers in the Monte Rosa massif (Pennine Alps). In some regions, such as the Ötztal Alps, EoS SLAs are relatively uniform between neighbouring glaciers, whereas in others - for example the Bernese Alps - distinct differences occur over short distances, with glaciers south of the main divide exhibiting notably higher EoS SLAs than those to the north. The bivariate analysis between multi-annual mean EoS SLA and glacier-specific parameters reveals no correlation with glacier area or mean slope (Fig. 6c,e). A geographic tendency towards lower EoS SLAs from west to east and from south to north across the Alps is present but statistically insignificant (Fig. 6a,b). As expected, EoS SLAs are substantially higher on south-facing glaciers than on north-facing ones (Fig. 6f), and they correlate strongly ($r^2 = 0.89$) with mean glacier elevation (Fig. 6d).

EoS SLA time series for selected glaciers illustrate strong interannual variability and significant long-term trends (Fig. 7). Extremely high EoS SLAs associated with the exceptional heat in the summers of 2022 and 2023 are clearly visible in several time series (Fig. 7). Conversely, the snow-rich winter of 2021 in the Bernese Alps is imprinted in the EoS SLA records of Kanderfirn, Grosser Aletschgletscher, Fieschergletscher, Unteraargletscher and Rhonegletscher (Fig. 7d-h). Long-term EoS

https://doi.org/10.5194/essd-2026-35
Preprint. Discussion started: 20 March 2026

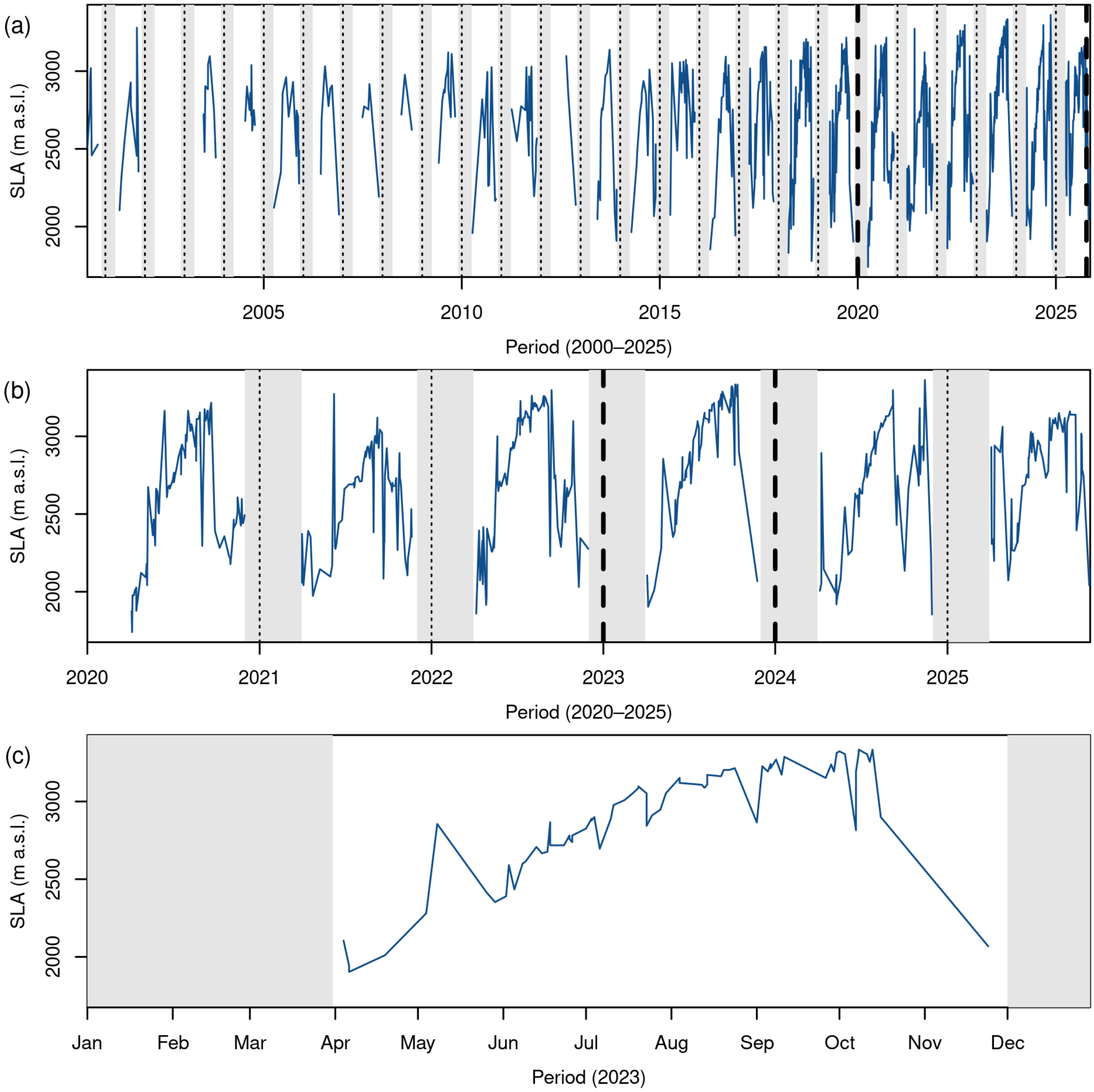

**Figure 4.** Temporal variations in the SLA during the ablation season on the Grosser Aletschgletscher, for three periods with different levels of detail: (a) 2000–2025, (b) 2020–2025, and (c) April–November 2023. Only scenes with a QA flag of 1 ("high confidence") were considered.

https://doi.org/10.5194/essd-2026-35
Preprint. Discussion started: 20 March 2026

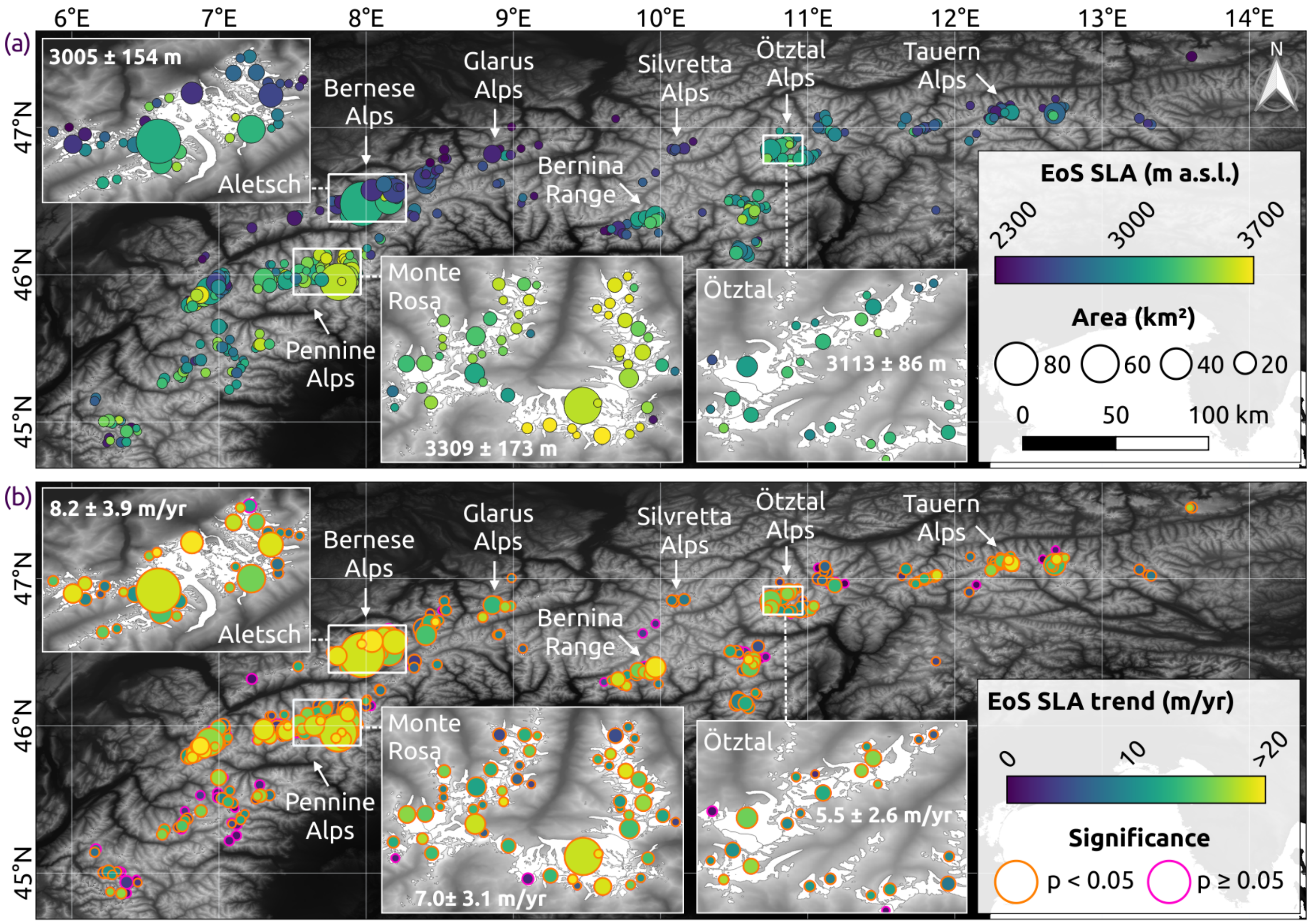

**Figure 5.** Overview maps showing: (a) the mean EoS SLA for all 405 glaciers considered across the Alps during the period 2000–2025, and (b) positive EoS SLA trends for 363 of these glaciers during the same period. The three insets show the Aletsch, Monte Rosa and Ötztal regions.

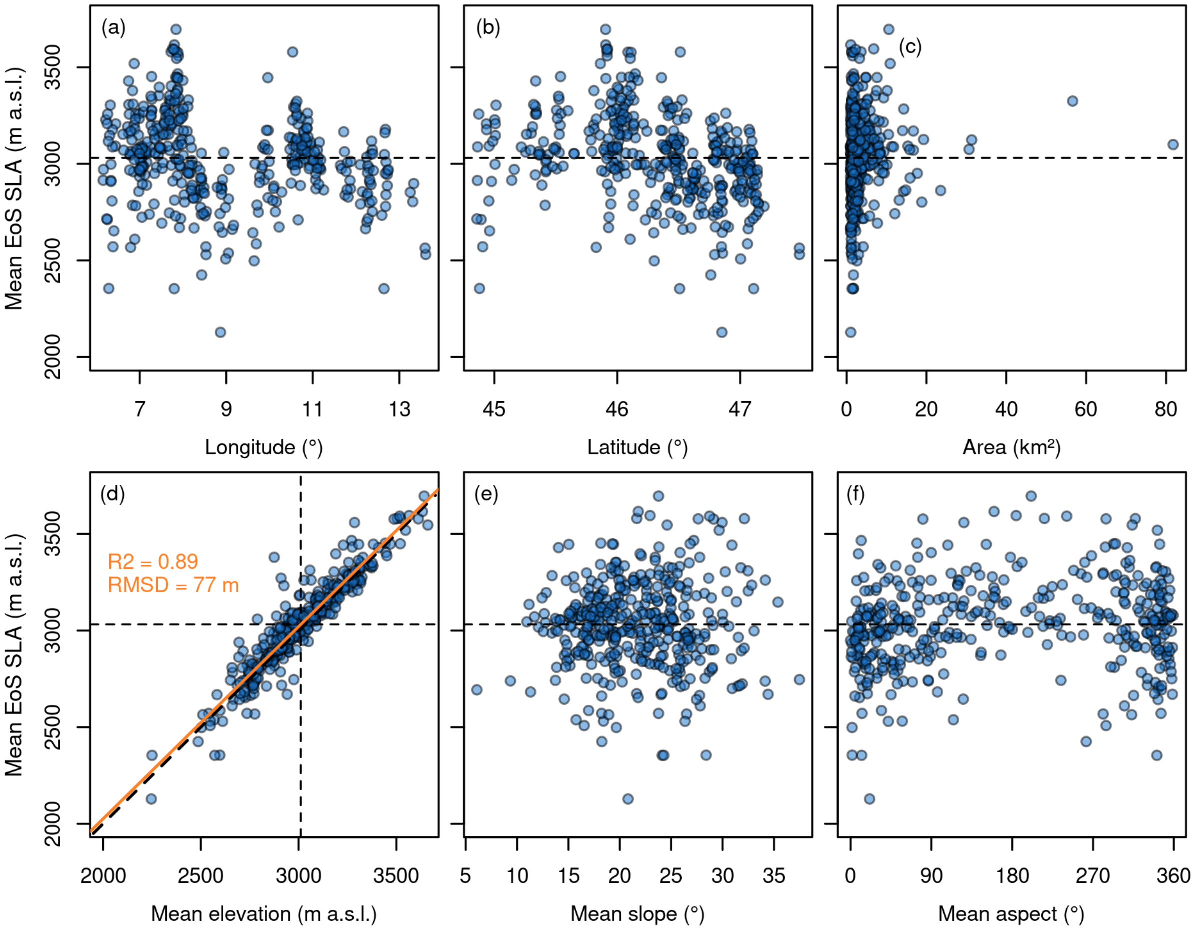

**Figure 6.** Bivariate analysis between multi-annual mean EoS SLA (2000-2025) and six different glacier-specific parameters: a) central longitude, b) central latitude, c) glacier area, d) mean elevation, e) mean slope, and f) mean aspect as extracted from RGI 7.0.

415 SLA trends range from ∼0 to more than 20 m year$^{-1}$ (Figs. 5 and 7), with spatial variability being pronounced both across the Alps and within individual mountain ranges (Fig. 5). The region-wide trend for 2000-2025 is 5.27 ± 4.54 m year$^{-1}$ when considering all glacier-specific trends (n = 398), 5.99 ± 4.00 m year$^{-1}$ when considering only positive trends (n = 363), and 6.61 ± 4.15 m year$^{-1}$ when only considering positive and significant trends (n = 306). Based on the region-wide annual mean EoS SLA anomaly time series (Section 3.6; Fig. 8), the long-term trend for the Alps is 5.59 m year$^{-1}$, corresponding to an average rise of ∼145 m during 2000-2025. 420

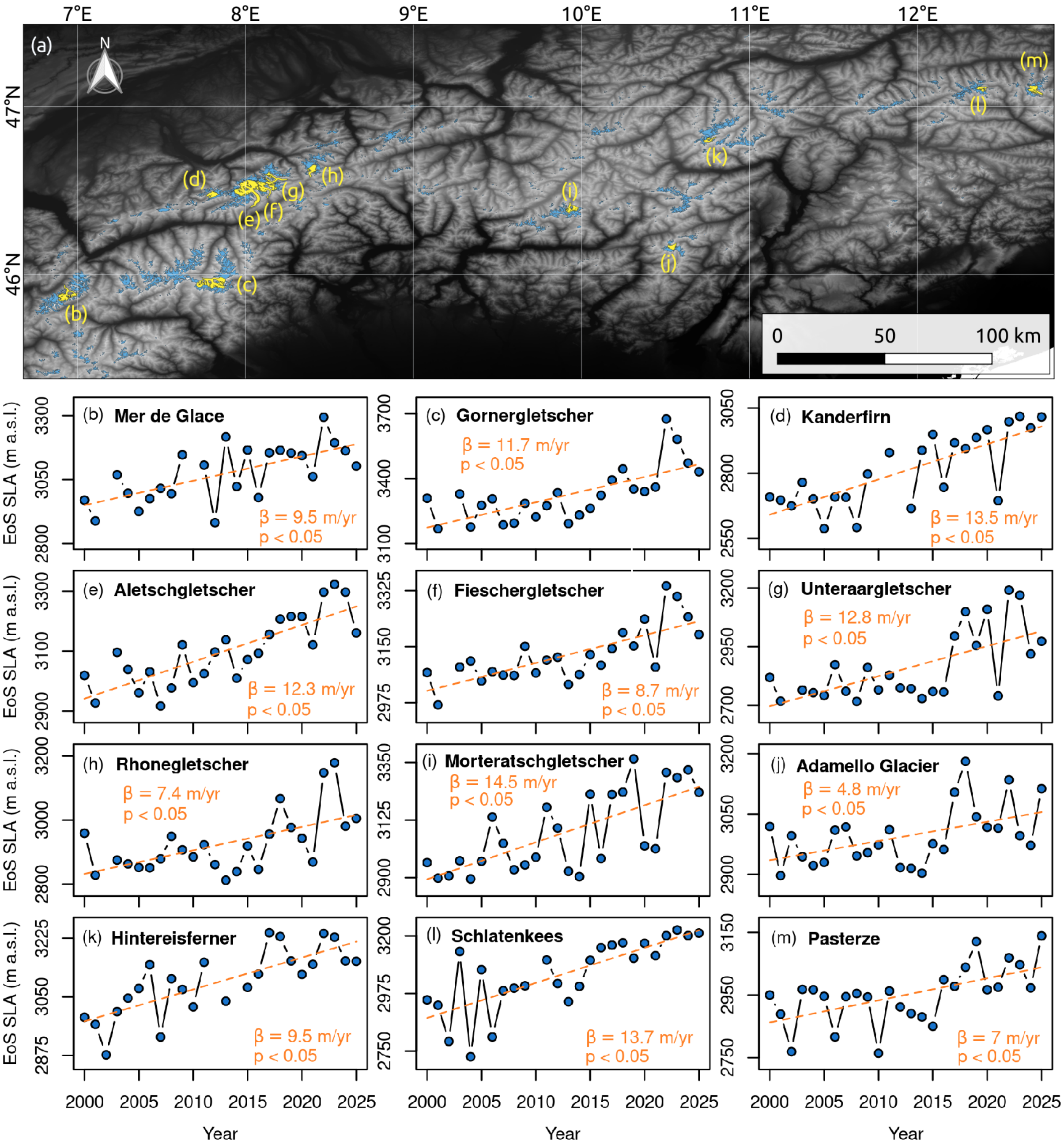

**Figure 7.** EoS SLA trends (2000–2025) for twelve glaciers across the Alps: (a) an overview map showing the location of the selected glaciers, and (b–m) EoS SLA time series for each glacier (2000–2025).

https://doi.org/10.5194/essd-2026-35
Preprint. Discussion started: 20 March 2026

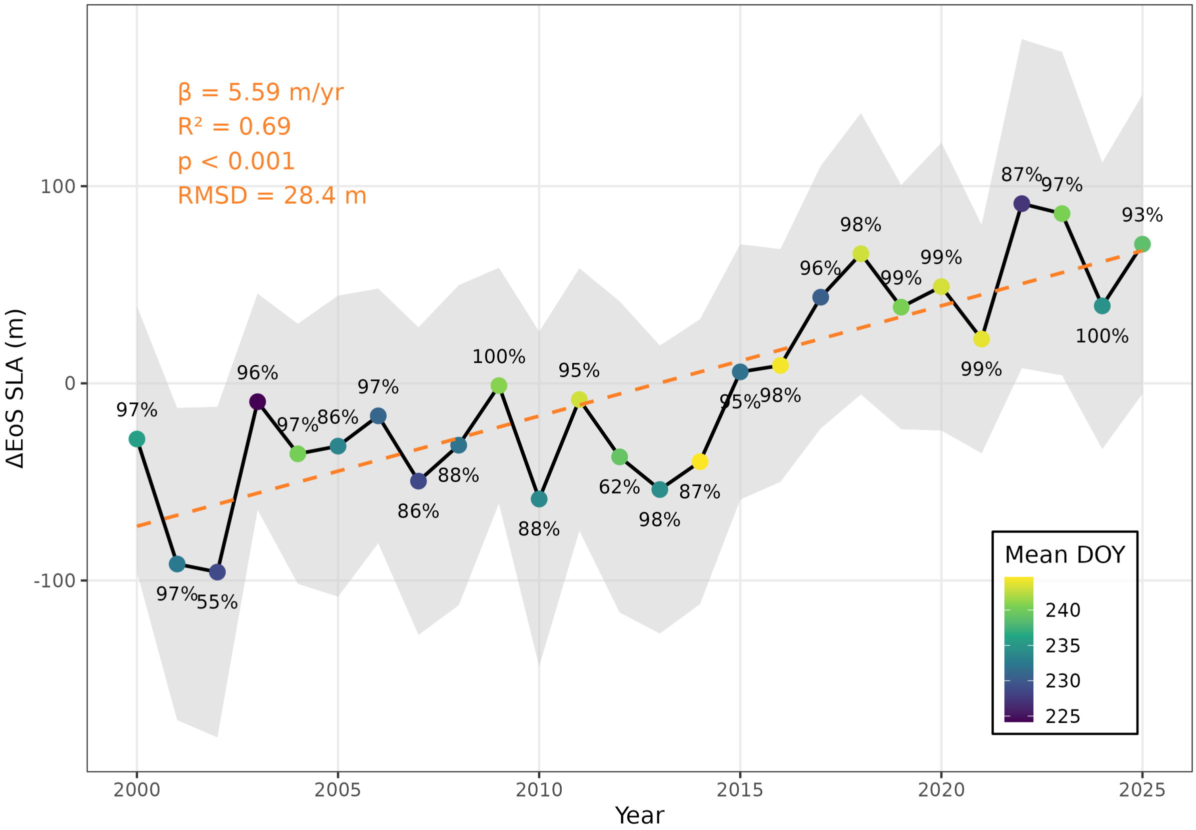

**Figure 8.** Glacier-specific EoS SLA trend for the Alps (2000-2025) based on region-wide annual mean anomalies (ΔEoS SLA). The anomaly was determined by calculating the relative EoS SLA deviation from the long-term mean (2000–2025) for each glacier and year with observations, and then taking the region-wide average. The dots are colour-coded according to the mean acquisition date (day of year, DOY) of all scenes from one ablation season that were used for calculating the EoS SLA anomaly. The percentage above or below each point indicates the proportion of the 405 considered glaciers for which the EoS SLA could be calculated in that respective year. The shaded area denotes the standard deviation of glacier-specific EoS SLA anomalies for each year.

## 5 Discussion

The aim of the following discussion is threefold: (i) to outline recent advancements and remaining uncertainties in automated snow line retrieval based on multi-mission satellite imagery, (ii) to place the new SLA observations from the Alps in the context of previous studies and (iii) to briefly discuss their potential for regional, data-driven glacier mass-balance simulations.

### 5.1 Automated glacier-specific snow line retrieval

As shown in the previous sections and Fig. 2, the temporal resolution of SLA measurements is controlled by the satellite acquisition density. For small glaciers or years with frequent cloud cover, the number of usable acquisitions per year sometimes drops to two or three before 2013. Data coverage was also impacted by the failure of the Landsat 7 ETM+ Scan Line Corrector (SLC), which introduced data voids after May 2003 and reduced the effective spatial scene coverage of glaciers not located at nadir view. This may affect the extraction of long-term trends for certain years or glaciers, such as EoS SLA, because it cannot be guaranteed that a satellite image representing the late summer maximum surface melt extent is available. However, trend extraction is likely to be much more robust for the last decade of the observation period because of significantly higher image acquisition repeat rates since the introduction of the Landsat-8 and -9 and Sentinel-2 mission data. This enables the detection of SLA dynamics, for example rapid SLA lowering by snowfall events followed by melt-induced SLA increases, when the glacier surface returns to its pre-snowfall state due to rising temperatures.

The main sources of uncertainty in the SLA detection workflow remain a lack of spatial coverage of the glacier surface by the satellite image and cloud contamination. Both effects can misrepresent the bimodal surface class distribution (snow and ice) in the reflectance histogram, resulting in an inaccurate threshold selection. The default cloud masks provided with Landsat and Sentinel-2 products were not applied as these frequently misclassify bright snow surfaces as clouds, which would result in the erroneous removal of pixels in areas of snow accumulation. Instead, cloud filtering was primarily based on NDSI thresholding, which effectively removes most cloud types, but cannot fully discriminate between clouds and snow due to their sometimes similar spectral characteristics. While scenes with complete cloud cover over the glacier surface can be often easily detected posterior based on the low variance of infrared reflectance values from homogeneous cloud cover, scenes with partial cloud cover are more challenging. When clouds obscure the ablation area, the reflectance contrast between cloud-covered ice and clear-sky snow in upper glacier regions can be misinterpreted as a snow line. This can cause an artificial increase in the estimated SLA for certain scenes. This effect can be observed for the SLAs of Grosser Aletschgletscher between May and June 2023, for example (Fig. 4).

Pixels enclosed by the RGI glacier outlines that are not covered by snow or ice may introduce additional uncertainty. Several RGI outlines include rocks or glacier ice covered by debris, which is either the result of glacier area retreat during the observation period or of debris-covered glaciers. Glacier areas with a high proportion of debris often show SLA detections during the early and late ablation periods when the debris is covered by seasonal snow. However, no valid observations are made during the peak melt period when the exposed debris is excluded by the NDSI band. Similar challenges are introduced by glacier retreat over the study period, as pixels at the glacier margin may no longer represent glacier ice, but instead bare rock or debris. The NDSI filtering of non-glacier pixels accounts for this dynamic change in the extent of glacierised areas. However, in some cases, this can result in a progressive reduction in the effective glacier area in later years of the time series, causing misleadingly low spatial coverage or erroneous flagging of observations as invalid. Since the RGI represents glacier extents of the early 21st century, changes in glacier area over time cannot be incorporated directly. Therefore, the total spatial coverage of a specific glacier and image must be treated carefully, particularly in the later years of the survey period. Otherwise, observations may be excluded if the outline no longer represents the current glacier geometry.

Changes in glacier surface elevation during the survey period additionally impact SLA estimation. The reference elevations used in this study are derived from the SRTM NASADEM, which reflects the glacier topography of the year 2000. However, given the substantial ice mass loss observed in the European Alps since then (e.g. Sommer et al., 2020; Hugonnet et al., 2021), using the SRTM surface elevations for the entire 26-year SLA time series would introduce a systematic bias into the long-term trends. Specifically, an observed increase in EoS SLA due to rising temperatures in the European Alps would be exaggerated because the glacier surface is lowering during the same period. To address this issue, a vertical correction has been applied using regional DEM differencing products (Hugonnet et al., 2021) to estimate the total elevation change at the location of the SLA at the time of image acquisition. It should be noted that this correction is based on the assumption of constant thinning rates between 2000 and 2019, since interannual or seasonal variations in thinning cannot be captured by the elevation change maps. Similarly, for years beyond 2019, we have to assume a continuation of constant elevation change rates because no more recent elevation change measurements are available for all Alpine glaciers.

In terms of glacier surface type classification, the Otsu thresholding method reliably distinguishes between snow-covered and snow-free pixels in most cases. However, it inherently forces a two-class split, even when surface reflectance exhibits a unimodal distribution. This can result in biased SLA retrieval when the glacier is completely snow-covered or snow-free. When the glacier is fully snow-covered, the algorithm may identify a boundary that is often biased upwards due to slightly darker pixels at the glacier terminus where thin snow cover overlies debris or rocks. This typically leads to an overestimation of the SLA at the beginning of the ablation period and the onset of surface melt at lower altitudes. Conversely, in late summer, when glaciers may be completely snow-free, the algorithm occasionally detects isolated patches of residual snow at high elevations. In these cases, there is often no continuous snow line present in the glacier's accumulation area anymore, resulting in a physically meaningless SLA estimate. Towards the end of the ablation season, the snow cover can be also entirely removed and the firn exposed. In these cases, the firn is often incorrectly classified as snow cover due to its different reflectance properties in comparison to melted ice. Distinct offsets between very high annual ELAs and EoS SLAs, as observed in Fig.A2, may also result from this false classification of firn. In addition to a lack of satellite image acquisitions at the end of the ablation period, the EoS SLA may not be representative of the ELA because the entire glacier was snow-free and exposed firn was classified as snow cover resulting in an underestimation of the EoS SLA.

Several previous studies have used optical remote sensing to estimate snow line elevations, exploiting the difference in infrared reflectance between glacier ice and snow. A number of recent studies have used a similar methodological approach to the one presented here, relying on Otsu thresholding Landsat imagery of selected glaciers in the European Alps (Rastner et al., 2019), High Mountain Asia, the Caucasus, western Canada (Li et al., 2022), the western Himalayas (Gaddam et al.,

2022) and the Southern Patagonian Icefield (Ortiz Diaz et al., 2024). In terms of optical data processing, these studies show some technical differences, e.g. cloud cover masking using thermal bands (Rastner et al., 2019) or the use of TOA instead of BOA data products (Loibl et al., 2025). Typically, the SLA was derived from a single DEM, assuming no glacier surface elevation change throughout the observation period. As (Rastner et al., 2019) demonstrated, assuming a constant glacier surface can introduce systematic biases of up to several dozen meters in SLA over decadal observation periods, which is similar to the mean elevation correction factor (∼30 m) observed here. Nevertheless, these studies demonstrated that the Otsu-based approach provides a robust, transferable classification method that compensates for brightness variations between sensors or acquisitions. The correlation between manually and automatically derived SLAs in this study ($r^2$ = 0.88) is comparable to or better than that reported in previous studies (Rastner et al., 2019; Li et al., 2022; Ortiz Diaz et al., 2024). As discussed at the beginning of this section, outliers were mainly observed in cases where the glacier surface was partially obscured by clouds, resulting in false separation. However, it is not possible to make a direct comparison of the SLAs retrieved because there are no automatically derived SLAs of glaciers in the Alps from other studies available. Another challenge in regionally observing SLAs over long survey periods is handling large amounts of remote sensing input data. Therefore, recent studies (Li et al., 2022; Ortiz Diaz et al., 2024) have developed respective workflows using the GEE cloud-processing platform, which offers direct access to ESA and NASA long-term data archives. In particular, the work presented by (Loibl et al., 2025) provided an operational processing pipeline for large-scale applications, e.g. regional SLA time series assessments. Our method has a similar objective, but instead of using a selection of empirically derived reflectance thresholds (Loibl et al., 2025), it is based on image- and glacier-specific reflectance thresholding. Additionally, the time series presented here provide a denser sampling of SLAs in recent years due to the inclusion of Sentinel-2 and allows to export the SLA and glacier snow cover masks as vector format files. In particular, the latter can provide valuable input data for further geospatial assessments, as it offers ready-to-use masks for partitioning the glacier surface into snow and ice.

### 5.2 Glacier-specific SLA variations

Driven by the steadily increasing availability of satellite imagery from multiple missions and advances in automated processing pipelines for snow-cover mapping on mountain glaciers (see Section 5.1), variations and trends in glacier-specific SLAs have been investigated with increasing intensity over recent years. Research has focused on several regions worldwide, with particular emphasis on the Alps (Rastner et al., 2019; Li et al., 2022) and the Pan-Tibetan Highlands, comprising the Himalaya, Karakoram, Tien Shan and Pamir (e.g. Barandun et al., 2018; Racoviteanu et al., 2019; Barandun et al., 2021; Li et al., 2022; Gaddam et al., 2022; Loibl et al., 2025). However, most existing studies concentrate either on individual glaciers (e.g. Barandun et al., 2018; Li et al., 2022; Ortiz Diaz et al., 2024) or on specific subregions within larger mountain ranges (e.g. Rastner et al., 2019; Racoviteanu et al., 2019; Gaddam et al., 2022). To date, region-wide datasets of consistent glacier-specific SLAs have been established only for the Qilian Mountains in China (Guo et al., 2021, $n_{\text{glaciers}} = 520$), the Southern Alps of New Zealand (Lorrey et al., 2022, $n_{\text{glaciers}} = 50$), and the Pan-Tibetan Highlands (Loibl et al., 2025, $n_{\text{glaciers}} \approx 28{,}000$). With the dataset presented here, we provide the first region-wide assessment of spatio-temporal SLA variations for glaciers across the Alps.

Previous studies focusing on the Alps investigated SLA changes for 26 glaciers in the Ötztal Alps using a total of 63 Landsat scenes (Rastner et al., 2019), and for six reference glaciers (Silvrettagletscher, Griesgletscher, Ghiacciaio del Careser, Hintereisferner, Kesselwandferner, and Vernagtferner) distributed across the Alps using approximately 100–300 Landsat scenes per glacier (Li et al., 2022). Rastner et al. (2019) reported a mean EoS SLA of 2979 m a.s.l. for the Ötztal Alps over the period 1985–2016, along with an increase of 57 m between 1985–2000 and 2001–2016. Based on our new dataset, the mean EoS SLA for glaciers in the Ötztal Alps ($n_{\text{glaciers}} = 21$) is 3113 ± 86 m a.s.l., which is clearly higher than the value reported by Rastner et al. (2019). This difference is plausible given the different, though partly overlapping, study periods (1985–2016 versus 2000–2025) and the pronounced increase of the local EoS SLA over time. The EoS SLA in the Ötztal Alps increased by 5.5 ± 2.6 m yr$^{-1}$, corresponding to a total rise of 143 ± 67 m between 2000 and 2025. The higher trend of 5.5 ± 2.6 m yr$^{-1}$ for the period 2000–2025 (this study) compared to the implied mean rate of 3.6 m yr$^{-1}$ derived from the step change of 57 m reported by Rastner et al. (2019), assuming a linear change between the midpoints of the two periods 1985–2000 and 2001–2016 (1992.5 and 2008.5; 16 years), indicates that the EoS SLA rise might have accelerated. Li et al. (2022) likewise identified increasing EoS SLAs for their six reference glaciers over the period 1985–2020, although no quantitative trend analysis was performed.

Mean EoS SLAs reported for other mountain regions worldwide exhibit substantial variability, reflecting regional differences in climate and glacier hypsometry. For example, the mean EoS SLA for glaciers in the Southern Alps of New Zealand is 1821 m a.s.l. (Lorrey et al., 2022, period 1981–2010, $n_{\text{glaciers}} = 50$), whereas it reaches 4779 ± 149 m a.s.l. in the Qilian Mountains of China (Guo et al., 2021, period 1989–2018, $n_{\text{glaciers}} = 520$). Even higher values of 5177 ± 108 m a.s.l. and 5444 ± 63 m a.s.l. have been reported for the Karakoram and the Eastern Himalaya, respectively (Racoviteanu et al., 2019, period 2000–2016, number of glaciers not specified). Similarly to the spatial patterns observed in the Alps (cf. Fig. 5), Guo et al. (2021) identified pronounced EoS SLA gradients across the Qilian Mountains, which they attributed to spatial variations in precipitation. Although no clear long-term EoS SLA trends have been reported for a subset of glaciers in the Karakoram (Racoviteanu et al., 2019), distinct upward trends comparable to those observed in the Alps (145 m from 2000 to 2025, equivalent to 5.6 m yr$^{-1}$; cf. Fig. 8) have been documented for other regions, including the Qilian Mountains (213 m from 1989 to 2018, equivalent to 7.1 m yr$^{-1}$; Guo et al., 2021) and the Southern Alps of New Zealand. Lorrey et al. (2022) reported a consistent rise in EoS SLA from the late 20th century to the present for the Southern Alps, with indications of a possible acceleration in recent years. Seasonal transient SLA variations, as illustrated for Grosser Aletschgletscher (cf. Fig. 4), have been addressed in only a few studies (c.f. Fig. 7 in Racoviteanu et al., 2019), likely owing to the limited availability of satellite scenes during the ablation season. Even comprehensive datasets such as that for the Pan-Tibetan Highlands (Loibl et al., 2025), which would enable region-wide analyses of EoS SLA trends and sub-seasonal SLA dynamics, have not yet been statistically explored in detail.

### 5.3 Relevance of SLA observations

Beyond their value for assessing the impacts of climate change on the mountain cryosphere, snow-covered area and transient SLA observations provide an independent and complementary data source to satellite-derived glacier elevation change and mass balance estimates. These observations can be used to better constrain model parameters during calibration. Multi-annual to multi-decadal mean geodetic mass balances derived from spaceborne satellite data (e.g. Sommer et al., 2020; Hugonnet et al., 2021) have become a widely used reference for glacier-specific mass balance model calibration in regional and global glacier projection studies (e.g. Rounce et al., 2023). In contrast, consistent region-wide SLA datasets, such as those presented in this study and by Loibl et al. (2025), offer a much higher temporal resolution and provide specific insights into snow accumulation processes and sub-seasonal mass balance variability (Barandun et al., 2018, 2021; Cremona et al., 2025). Snow-covered area fraction, which is used in some studies for glacier mass balance model calibration (e.g. Cremona et al., 2025), avoids the need for additional data sources (i.e. DEMs) required for SLA retrieval. However, it is sensitive to changes in glacier area and requires consistency between the glacier outlines used for snow cover mapping and those applied in mass balance modelling. A key advantage of transient SLA observations is that they can be readily implemented as calibration targets in flowline models of reduced geometric complexity, as well as in distributed or fully three-dimensional glacier models.

Although a combined calibration approach using geodetic mass balance data together with snow cover or transient SLA observations alone will not resolve the fundamental issues of model over-parameterisation and equifinality (cf. Rounce et al., 2020; Schuster et al., 2023), which arise from the imbalance between the number of model parameters and available observations, the additional information nevertheless shows considerable potential for improving the representation of accumulation rates, mass balance gradients, and meltwater runoff (Barandun et al., 2018, 2021; Cremona et al., 2025). This is important given the large precipitation-related uncertainties in complex terrain, which arise from the lack of high-altitude weather stations, gauge undercatch, the coarse resolution of global climate models, and the poor parameterization of sub-grid processes in regional climate models (e.g. Pepin et al., 2022). Other regional satellite-derived datasets, such as glacier albedo products, are becoming increasingly available and represent a promising additional source for enhancing data-driven surface mass balance modelling (e.g. Naegeli et al., 2017, 2019; Feng et al., 2024; Ren et al., 2024; Xie et al., 2024). At present, however, the main bottleneck for the integration of such satellite-derived information into glacier modelling remains the lack of consistent regional- to global-scale datasets. The cloud-based processing approaches applied in this study and in recent work (e.g. Li et al., 2022; Loibl et al., 2025; Feng et al., 2024; Ren et al., 2024; Xie et al., 2024) substantially alleviate this limitation by enabling the efficient processing of large volumes of satellite imagery, thereby opening new opportunities for the generation of regional to global glacier-specific data products.

## 6 Conclusions

In the European Alps, we measured approximately 200,000 SLAs for 408 glaciers, representing roughly 75 % of the total glacierized area, over the period 2000–2025. SLAs are significantly correlated with mean glacier elevation and exposition. Trend analysis of annual SLAs indicates a mean regional increase in snow line of approximately 6 m year$^{-1}$, accompanied by strong interannual variability such as years with extreme summer melt.

Our workflow incorporates image-specific masking procedures to exclude reflectance values of pixels which are neither snow or ice. In addition, glacier elevation change due to surface melt is compensated through a vertical correction using glacier elevation change maps. Thereby, robust SLA retrieval and interannual consistency throughout the observation period is ensured for glaciers with heavy debris cover, significant area retreat or substantial surface lowering. Uncertainties are caused primarily by satellite images with low spatial coverage or undetected clouds, which result in biased reflectance histograms and consequently an inaccurate separation of snow and ice. Systematic offsets are also observed for acquisitions at the beginning and end of the ablation season, when snow and ice boundaries are spatially fragmented. These conditions lead to a slight overestimation of SLA at the onset of surface melt and an underestimation during late-summer. Nevertheless, the comparison of SLA estimates between different remote sensing sensors and against visually delineated reference snow lines show a high level of accuracy in most cases with a mean error (RMSE) of approximately 100 m.

The sampling density of SLA measurements varies considerably between years, which limits the observation of seasonal SLA change during the early 21st century. However, the introduction of Sentinel-2, in combination with Landsat-8 and Landsat-9, substantially increases the temporal resolution of observations from the mid-2010s onward, allowing revisit intervals of a few days. Overall, our approach allows the efficient analysis of glacier snow cover and SLAs at regional scales. Continued observations from the current Sentinel-2 and Landsat missions, will also further enhance the observation of intra- and inter-annual SLA change. In light of global warming and glacier retreat, transient SLA series with high temporal resolution have great potential to improve projections of glacier change. This is because, when combined with other remote sensing observations, temporal SLA information can be used to constrain surface mass balance gradients, thereby enhancing projections of glacier-specific to regional ice mass loss and meltwater runoff.

## 7 Code and data availability

Glacier-specific SLA time series, estimated end-of-summer snow lines, trend statistics and geopackages of spatial SLA masks per glacier are available at Zenodo (https://doi.org/10.5281/zenodo.18223929; Sommer et al. (2026)). The SLA retrival code in Google Earth Engine and all other postprocessing code can be accessed via the GitHub repository "snowy-glaciers" (https://github.com/cr-sommer/snowy-glaciers).

## Appendix A

### A1

https://doi.org/10.5194/essd-2026-35
Preprint. Discussion started: 20 March 2026

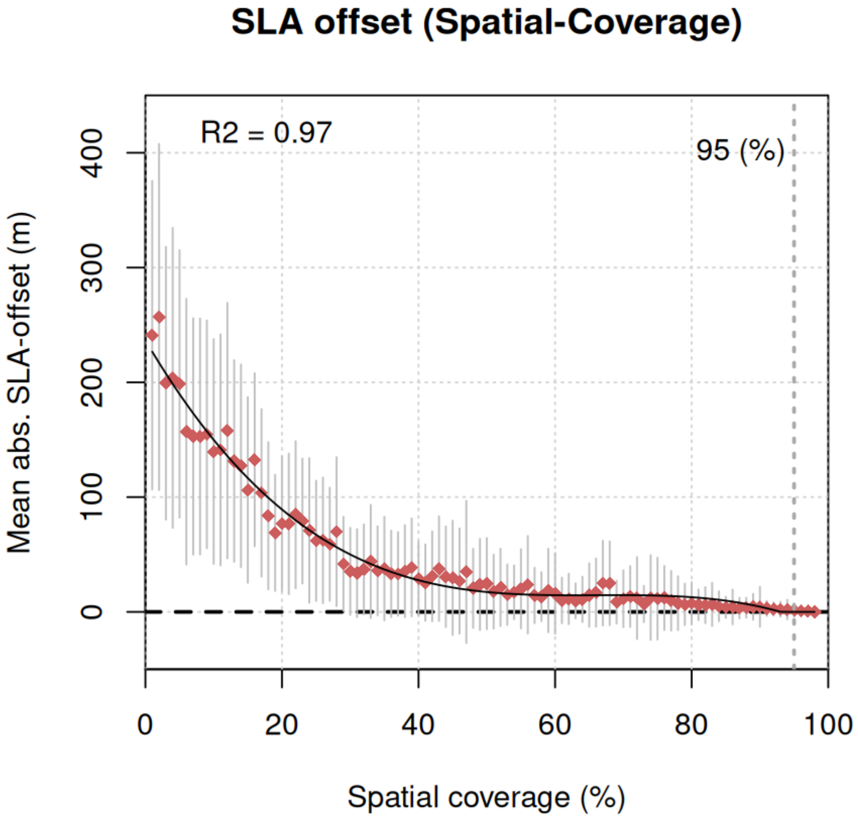

**Figure A1.** Mean absolute vertical difference between SLA measurements derived from full available spatial coverage of satellite images and reduced spatial coverage by creating artificial data voids across the glacier surface. Mean absolute SLA offsets (red squares) are aggregated based on 1 % bins of area covered. The standard deviation of each bin is shown as gray vertical lines. The black solid line ($r^2$=0.97) indicates the correlation between relative spatial coverage of the glacier surface and vertical SLA offset as used to estimate the error contribution of specific SLA measurements from the area covered. For SLA measurements with a coverage of more than 95 %, the function is coerced to 0 meters.

https://doi.org/10.5194/essd-2026-35
Preprint. Discussion started: 20 March 2026

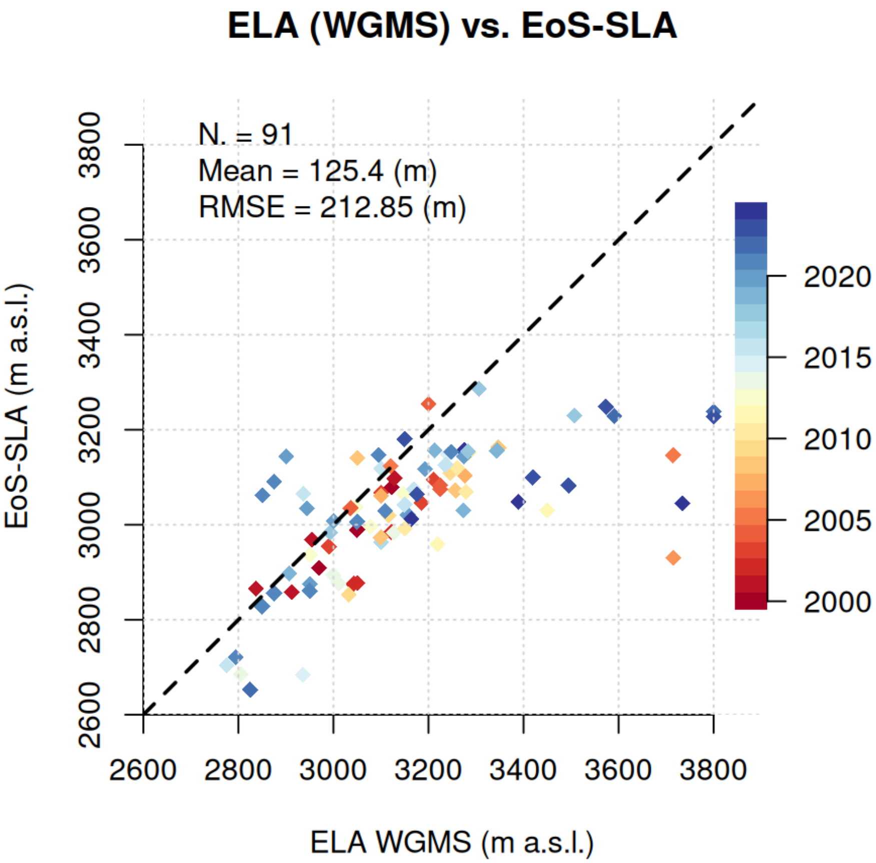

**Figure A2.** Comparison of end-of-summer SLA estimates and annual equilibrium line altitudes (ELA) of glaciers in the Alps provided by WGMS.

**Table A1.** Remote sensing datasets used in this study: Sensor, acquisition periods, number of images, spatial resolution (Res.) and data products identifiers

| Mission | Sensor | Period | N. images | Res. [m] | GEE data ID |
|---|---|---|---|---|---|
| Landsat-5 (LT05) | TM | 2000-2011 | 888 | 30 | LANDSAT/LT05/C02/T1_L2 |
| Landsat-7 (LE07) | ETM+ | 2000-2023 | 2487 | 30 | LANDSAT/LE07/C02/T1_L2 |
| Landsat-8 (LC08) | OLI | 2013-2025 | 1784 | 30 | LANDSAT/LC08/C02/T1_L2 |
| Landsat-9 (LC09) | OLI-2 | 2021-2025 | 559 | 30 | LANDSAT/LC09/C02/T1_L2 |
| Sentinel-2 (S2) | MSI | 2017-2025 | 7736 | 10-20 | COPERNICUS/S2_SR_HARMONIZED |
| SRTM-NASADEM | C-SAR | 2000 | - | 30 | NASA/NASADEM_HGT/001 |

https://doi.org/10.5194/essd-2026-35
Preprint. Discussion started: 20 March 2026

**Table A2.** Reference glaciers with manually delineated SLAs: Glacier area (Area) and elevation range (Elev.) are extracted from RGI7.0. N. SLA denotes number of visually mapped snow lines per glacier. Mean, standard deviation (SD) and root mean square error (RMSE) indicate glacier-specific deviations between manual and automatic SLA observation.

| RGI ID | Name | Area [km$^2$] | Elev. [m a.s.l.] | N. SLA | Mean [m] | SD [m] | RMSE [m] |
|---|---|---|---|---|---|---|---|
| RGI2000-v7.0-G-11-00448 | Tsanteleina | 3.12 | 2709-3413 | 47 | 3.00 | 44.10 | 43.73 |
| RGI2000-v7.0-G-11-00678 | Trelatete | 8.36 | 2031-3835 | 23 | -26.70 | 102.27 | 103.52 |
| RGI2000-v7.0-G-11-00732 | Saleinaz | 7.08 | 1827-3865 | 46 | -56.30 | 98.38 | 112.42 |
| RGI2000-v7.0-G-11-00757 | Mer de Glace | 30.66 | 1526-4040 | 33 | -22.27 | 114.66 | 115.09 |
| RGI2000-v7.0-G-11-00823 | Corbassiere | 16.72 | 2235-4278 | 44 | -142.14 | 205.09 | 247.61 |
| RGI2000-v7.0-G-11-00922 | Zinal | 14.03 | 2032-3924 | 55 | 84.69 | 99.58 | 130.04 |
| RGI2000-v7.0-G-11-01182 | Allalin | 9.28 | 2621-4158 | 52 | -23.79 | 83.47 | 86.02 |
| RGI2000-v7.0-G-11-01189 | Findelgletscher | 14.31 | 2509-3768 | 31 | 13.00 | 52.28 | 53.05 |
| RGI2000-v7.0-G-11-01457 | Kanderfirn | 13.17 | 2253-3215 | 83 | 27.81 | 110.14 | 112.95 |
| RGI2000-v7.0-G-11-01706 | Rhonegletscher | 15.90 | 2218-3594 | 80 | -7.50 | 129.13 | 128.54 |
| RGI2000-v7.0-G-11-02216 | Morteratsch | 15.81 | 2030-3975 | 38 | 4.68 | 161.71 | 159.64 |
| RGI2000-v7.0-G-11-02438 | Griesgletscher | 5.43 | 2417-3301 | 14 | -11.07 | 81.60 | 79.41 |
| RGI2000-v7.0-G-11-02596 | Aletschgletscher | 81.78 | 1583-4114 | 55 | -59.35 | 74.86 | 95.00 |
| RGI2000-v7.0-G-11-02645 | Unteraar | 23.55 | 1940-3926 | 45 | 61.98 | 70.13 | 93.00 |
| RGI2000-v7.0-G-11-02875 | Langen | 2.16 | 2689-3400 | 31 | 35.42 | 102.47 | 106.85 |
| RGI2000-v7.0-G-11-03116 | Hintereis | 8.04 | 2434-3693 | 60 | -14.07 | 100.91 | 101.05 |
| RGI2000-v7.0-G-11-03215 | Taschachferner | 5.36 | 2252-3728 | 34 | 17.97 | 80.79 | 81.60 |
| RGI2000-v7.0-G-11-03239 | Gepatschferner | 16.72 | 2122-3494 | 23 | -34.00 | 104.55 | 107.76 |
| RGI2000-v7.0-G-11-03356 | Fernerstube | 1.57 | 2501-3244 | 18 | 98.56 | 27.51 | 102.12 |
| RGI2000-v7.0-G-11-03456 | Gurglerferner | 8.97 | 2460-3397 | 18 | 27.11 | 50.58 | 56.13 |
| RGI2000-v7.0-G-11-03664 | Pasterze | 17.71 | 2089-3504 | 20 | 45.20 | 104.17 | 111.13 |
| RGI2000-v7.0-G-11-03808 | Schlatenkees | 8.27 | 2144-3572 | 28 | -19.04 | 109.37 | 109.07 |
| RGI2000-v7.0-G-11-03953 | Hornkees | 2.37 | 2214-3235 | 30 | 8.13 | 73.67 | 72.88 |

https://doi.org/10.5194/essd-2026-35
Preprint. Discussion started: 20 March 2026

**Table A3.** Sensor-specific comparison of SLA measurements with a maximum time difference of 1 day. Number of pairwise differences (N. pairs) and mean time difference in days (Mean days) are stated for each pair of satellites (Sensor pairs). 05 % SLA-off. and 95 % SLA-off. denote the 5 and 95 % percentiles of absolute SLA differences between sensor pairs.

| Sensor pairs | N. pairs | Mean days | Mean abs. [m] | RMSE [m] | 05 % SLA-off. [m] | 95 % SLA-off. [m] |
|---|---|---|---|---|---|---|
| LC08 - LC09 | 6917 | 1.00 | 53.34 | 89.11 | 0.00 | 219.84 |
| LC08 - LE07 | 10824 | 0.96 | 60.52 | 92.00 | 0.42 | 216.55 |
| LC08 - S2SR | 23524 | 0.59 | 54.46 | 89.32 | 0.00 | 217.39 |
| LC09 - LE07 | 1475 | 0.61 | 54.41 | 88.14 | 0.22 | 217.95 |
| LC09 - S2SR | 11085 | 0.61 | 54.32 | 89.33 | 0.00 | 216.95 |
| LE07 - LT05 | 4496 | 1.00 | 65.66 | 95.87 | 0.21 | 223.57 |
| LE07 - S2SR | 13805 | 0.57 | 56.79 | 86.90 | 0.23 | 200.47 |

*Author contributions.* CS and ARG conceived the study. CS developed the cloud-based processing algorithms, implemented the snow cover mapping and snow line altitude retrieval on the Google Earth Engine geospatial data analysis platform, processed the satellite data and conducted the data uncertainty analysis. ARG contributed to the refinement of the workflow, computed glacier-specific end-of-summer snow line altitudes, and performed the statistical analyses. CS and ARG drafted the manuscript and prepared the figures. JJF and MB provided valuable feedback and contributed to the revision of the manuscript.

*Competing interests.* The authors declare that they have no competing interests.

*Acknowledgements.* We thank Ronja Lilienweiß and Korbinian Müller for their support in the manual mapping of transient snowline altitudes on glaciers in the Alps, NASA and ESA for the provision of freely available satellite imagery, and Google Earth Engine for the noncommercial cloud processing and storage capacities.

*Financial support.* CS acknowledges the financial support received from the Dr. Hertha & Helmut Schmauser Research Foundation for cloud-based data processing within the framework of the funded research project "Automated measurement of seasonal snow cover on glaciers using time-series analysis of optical satellite data in Google Earth Engine". ARG and JJF received primary funding from the European Union’s Horizon 2020 research and innovation programme via the European Research Council (ERC) as a Starting Grant (FRAGILE project) under grant agreement No. 948290.

## References

Barandun, M., Huss, M., Usubaliev, R., Azisov, E., Berthier, E., Kääb, A., Bolch, T., and Hoelzle, M.: Multi-decadal mass balance series of three Kyrgyz glaciers inferred from modelling constrained with repeated snow line observations, The Cryosphere, 12, 1899–1919, https://doi.org/10.5194/tc-12-1899-2018, 2018.

Barandun, M., Pohl, E., Naegeli, K., McNabb, R., Huss, M., Berthier, E., Saks, T., and Hoelzle, M.: Hot Spots of Glacier Mass Balance Variability in Central Asia, Geophysical Research Letters, 48, e2020GL092 084, https://doi.org/10.1029/2020GL092084, 2021.

Chander, G., Markham, B. L., and Helder, D. L.: Summary of current radiometric calibration coefficients for Landsat MSS, TM, ETM+, and EO-1 ALI sensors, Remote Sensing of Environment, 113, 893–903, https://doi.org/10.1016/j.rse.2009.01.007, 2009.

Chastain, R., Housman, I., Goldstein, J., Finco, M., and Tenneson, K.: Empirical cross sensor comparison of Sentinel-2A and 2B MSI, Landsat-8 OLI, and Landsat-7 ETM+ top of atmosphere spectral characteristics over the conterminous United States, Remote Sensing of Environment, 221, 274–285, https://doi.org/10.1016/j.rse.2018.11.012, 2019.

Choi, H.: Cloud detection in Landsat imagery of ice sheets using shadow matching technique and automatic normalized difference snow index threshold value decision, Remote Sensing of Environment, 91, 237–242, https://doi.org/10.1016/j.rse.2004.03.007, 2004.

Corripio, J. G.: Vectorial algebra algorithms for calculating terrain parameters from DEMs and solar radiation modelling in mountainous terrain, International Journal of Geographical Information Science, 17, 1–23, https://doi.org/10.1080/713811744, 2003.

Cremona, A., Huss, M., Landmann, J. M., Schwaizer, G., Paul, F., and Farinotti, D.: Constraining sub-seasonal glacier mass balance in the Swiss Alps using Sentinel-2-derived snow-cover observations, Journal of Glaciology, 71, e25, https://doi.org/10.1017/jog.2025.1, 2025.

Crippen, R., Buckley, S., Agram, P., Belz, E., Gurrola, E., Hensley, S., Kobrick, M., Lavalle, M., Martin, J., Neumann, M., Nguyen, Q., Rosen, P., Shimada, J., Simard, M., and Tung, W.: NASADEM GLOBAL ELEVATION MODEL: METHODS AND PROGRESS, ISPRS - International Archives of the Photogrammetry, Remote Sensing and Spatial Information Sciences, XLI-B4, 125–128, https://doi.org/10.5194/isprsarchives-XLI-B4-125-2016, 2016.

Davaze, L., Rabatel, A., Dufour, A., Hugonnet, R., and Arnaud, Y.: Region-Wide Annual Glacier Surface Mass Balance for the European Alps From 2000 to 2016, Frontiers in Earth Science, 8, 149, https://doi.org/10.3389/feart.2020.00149, 2020.

Dell, R. L., Banwell, A. F., Willis, I. C., Arnold, N. S., Halberstadt, A. R. W., Chudley, T. R., and Pritchard, H. D.: Supervised classification of slush and ponded water on Antarctic ice shelves using Landsat 8 imagery, 68, 401–414, https://doi.org/10.1017/jog.2021.114, 2022.

Dozier, J., Bair, E. H., Baskaran, L., Brodrick, P. G., Carmon, N., Kokaly, R. F., Miller, C. E., Miner, K. R., Painter, T. H., and Thompson, D. R.: Error and Uncertainty Degrade Topographic Corrections of Remotely Sensed Data, Journal of Geophysical Research: Biogeosciences, 127, e2022JG007 147, https://doi.org/10.1029/2022JG007147, 2022.

Drusch, M., Del Bello, U., Carlier, S., Colin, O., Fernandez, V., Gascon, F., Hoersch, B., Isola, C., Laberinti, P., Martimort, P., Meygret, A., Spoto, F., Sy, O., Marchese, F., and Bargellini, P.: Sentinel-2: ESA's Optical High-Resolution Mission for GMES Operational Services, Remote Sensing of Environment, 120, 25–36, https://doi.org/10.1016/j.rse.2011.11.026, 2012.

EEA: Fractional Snow Cover 2016-present (raster 20 m), Europe, daily, https://sdi.eea.europa.eu/catalogue/copernicus/api/records/3e2b4b7b-a460-41dd-a373-962d032795f3?language=all, https://doi.org/10.2909/3e2b4b7b-a460-41dd-a373-962d032795f3, accessed: 2025-11-21, 2025.

ESA: European Space Agency - Copernicus Sentinel-2 (processed by ESA), 2021, MSI Level-2A BOA Reflectance Product. Collection 1., https://doi.org/https://doi.org/10.5270/S2_-znk9xsj, 2021.

Farr, T. G., Rosen, P. A., Caro, E., Crippen, R., Duren, R., Hensley, S., Kobrick, M., Paller, M., Rodriguez, E., Roth, L., Seal, D., Shaffer, S., Shimada, J., Umland, J., Werner, M., Oskin, M., Burbank, D., and Alsdorf, D.: The Shuttle Radar Topography Mission, Reviews of Geophysics, 45, 2005RG000 183, https://doi.org/10.1029/2005RG000183, 2007.

Feng, S., Cook, J. M., Onuma, Y., Naegeli, K., Tan, W., Anesio, A. M., Benning, L. G., and Tranter, M.: Remote sensing of ice albedo using harmonized Landsat and Sentinel 2 datasets: validation, International Journal of Remote Sensing, 45, 7724–7752, https://doi.org/10.1080/01431161.2023.2291000, 2024.

Florath, J., Keller, S., Abarca-del Rio, R., Hinz, S., Staub, G., and Weinmann, M.: Glacier Monitoring Based on Multi-Spectral and Multi-Temporal Satellite Data: A Case Study for Classification with Respect to Different Snow and Ice Types, Remote Sensing, 14, 845, https://doi.org/10.3390/rs14040845, 2022.

Franks, S., Storey, J., and Rengarajan, R.: The New Landsat Collection-2 Digital Elevation Model, Remote Sensing, 12, 3909, https://doi.org/10.3390/rs12233909, 2020.

Gaddam, V. K., Boddapati, R., Kumar, T., Kulkarni, A. V., and Bjornsson, H.: Application of "OTSU"—an image segmentation method for differentiation of snow and ice regions of glaciers and assessment of mass budget in Chandra basin, Western Himalaya using Remote Sensing and GIS techniques, Environmental Monitoring and Assessment, 194, 337, https://doi.org/10.1007/s10661-022-09945-2, 2022.

Gascoin, S., Grizonnet, M., Bouchet, M., Salgues, G., and Hagolle, O.: Theia Snow collection: high-resolution operational snow cover maps from Sentinel-2 and Landsat-8 data, Earth System Science Data, 11, 493–514, https://doi.org/10.5194/essd-11-493-2019, 2019.

Gascon, F., Bouzinac, C., Thépaut, O., Jung, M., Francesconi, B., Louis, J., Lonjou, V., Lafrance, B., Massera, S., Gaudel-Vacaresse, A., Languille, F., Alhammoud, B., Viallefont, F., Pflug, B., Bieniarz, J., Clerc, S., Pessiot, L., Trémas, T., Cadau, E., De Bonis, R., Isola, C., Martimort, P., and Fernandez, V.: Copernicus Sentinel-2A Calibration and Products Validation Status, Remote Sensing, 9, 584, https://doi.org/10.3390/rs9060584, 2017.

GCOS: Essential Climate Variables, https://gcos.wmo.int/site/global-climate-observing-system-gcos/essential-climate-variables, accessed: 2025-11-20, 2025.

Guo, Z., Wang, N., Shen, B., Gu, Z., Wu, Y., and Chen, A.: Recent Spatiotemporal Trends in Glacier Snowline Altitude at the End of the Melt Season in the Qilian Mountains, China, Remote Sensing, 13, 4935, https://doi.org/10.3390/rs13234935, 2021.

Hall, D., Ormsby, J., Bindschadler, R., and Siddalingaiah, H.: Characterization of Snow and Ice Reflectance Zones On Glaciers Using Landsat Thematic Mapper Data, Annals of Glaciology, 9, 104–108, https://doi.org/10.3189/S0260305500000471, 1987.

Hall, D. K., Riggs, G. A., and Salomonson, V. V.: Development of methods for mapping global snow cover using moderate resolution imaging spectroradiometer data, Remote Sensing of Environment, 54, 127–140, https://doi.org/10.1016/0034-4257(95)00137-P, 1995.

Hugonnet, R., McNabb, R., Berthier, E., Menounos, B., Nuth, C., Girod, L., Farinotti, D., Huss, M., Dussaillant, I., Brun, F., and Kääb, A.: Accelerated global glacier mass loss in the early twenty-first century, Nature, 592, 726–731, https://doi.org/10.1038/s41586-021-03436-z, 2021.

Huss, M.: Present and future contribution of glacier storage change to runoff from macroscale drainage basins in Europe, Water Resources Research, 47, https://doi.org/10.1029/2010WR010299, number: 7, 2011.

Huss, M. and Hock, R.: Global-scale hydrological response to future glacier mass loss, Nature Climate Change, 8, 135–140, https://doi.org/10.1038/s41558-017-0049-x, 2018.

Immerzeel, W. W., Lutz, A. F., Andrade, M., Bahl, A., Biemans, H., Bolch, T., Hyde, S., Brumby, S., Davies, B. J., Elmore, A. C., Emmer, A., Feng, M., Fernández, A., Haritashya, U., Kargel, J. S., Koppes, M., Kraaijenbrink, P. D. A., Kulkarni, A. V., Mayewski, P. A., Nepal, S., Pacheco, P., Painter, T. H., Pellicciotti, F., Rajaram, H., Rupper, S., Sinisalo, A., Shrestha, A. B., Viviroli, D., Wada, Y., Xiao, C., Yao, T., and Baillie, J. E. M.: Importance and vulnerability of the world's water towers, Nature, 577, 364–369, https://doi.org/10.1038/s41586-019-1822-y, number: 7790, 2020.

Irons, J. R. and Dwyer, J. L.: An overview of the Landsat Data Continuity Mission, SPIE Defense, Security, and Sensing, p. 769508, https://doi.org/10.1117/12.850416, 2010.

JPL, N.: NASADEM Merged DEM Global 1 arc second V001 [Data set], https://doi.org/https://doi.org/10.5067/MEASURES/NASADEM/NASADEM_HGT.001, 2020.

Kaewmanee, M., Leigh, L., Shah, R., and Gross, G.: Inter-Comparison of Landsat-8 and Landsat-9 during On-Orbit Initialization and Verification (OIV) Using Extended Pseudo Invariant Calibration Sites (EPICS): Advanced Methods, Remote Sensing, 15, 2330, https://doi.org/10.3390/rs15092330, 2023.

Korzeniowska, K., Bühler, Y., Marty, M., and Korup, O.: Regional snow-avalanche detection using object-based image analysis of near-infrared aerial imagery, Natural Hazards and Earth System Sciences, 17, 1823–1836, https://doi.org/10.5194/nhess-17-1823-2017, 2017.

Larocca, L. J., Lea, J. M., Erb, M. P., McKay, N. P., Phillips, M., Lamantia, K. A., and Kaufman, D. S.: Arctic glacier snowline altitudes rise 150 m over the last 4 decades, The Cryosphere, 18, 3591–3611, https://doi.org/10.5194/tc-18-3591-2024, 2024.

Li, X., Wang, N., and Wu, Y.: Automated Glacier Snow Line Altitude Calculation Method Using Landsat Series Images in the Google Earth Engine Platform, Remote Sensing, 14, 2377, https://doi.org/10.3390/rs14102377, 2022.

Loibl, D., Richter, N., and Grünberg, I.: Remote sensing-derived time series of transient glacier snowline altitudes for High Mountain Asia, 1985–2021, Scientific Data, 12, 103, https://www.nature.com/articles/s41597-024-04309-6, 2025.

Lorrey, A. M., Vargo, L., Purdie, H., Anderson, B., Cullen, N. J., Sirguey, P., Mackintosh, A., Willsman, A., Macara, G., and Chinn, W.: Southern Alps equilibrium line altitudes: four decades of observations show coherent glacier–climate responses and a rising snowline trend, Journal of Glaciology, 68, 1127–1140, https://doi.org/10.1017/jog.2022.27, 2022.

Lutz, A. F., Immerzeel, W. W., Siderius, C., Wijngaard, R. R., Nepal, S., Shrestha, A. B., Wester, P., and Biemans, H.: South Asian agriculture increasingly dependent on meltwater and groundwater, Nature Climate Change, 12, 566–573, https://doi.org/10.1038/s41558-022-01355-z, 2022.

Main-Knorn, M., Pflug, B., Louis, J., Debaecker, V., Müller-Wilm, U., and Gascon, F.: Sen2Cor for Sentinel-2, in: Image and Signal Processing for Remote Sensing XXIII, edited by Bruzzone, L., Bovolo, F., and Benediktsson, J. A., SPIE, Warsaw, Poland, https://doi.org/10.1117/12.2278218, 2017.

Martín-Ortega, P., García-Montero, L. G., and Sibelet, N.: Temporal Patterns in Illumination Conditions and Its Effect on Vegetation Indices Using Landsat on Google Earth Engine, Remote Sensing, 12, 211, https://doi.org/10.3390/rs12020211, 2020.

Matzl, M. and Schneebeli, M.: Measuring specific surface area of snow by near-infrared photography, Journal of Glaciology, 52, 558–564, https://doi.org/10.3189/172756506781828412, 2006.

Mizuochi, H., Sasagawa, T., Ito, A., Iijima, Y., Park, H., Nagano, H., Ichii, K., and Hiyama, T.: Creation and environmental applications of 15-year daily inundation and vegetation maps for Siberia by integrating satellite and meteorological datasets, Progress in Earth and Planetary Science, 11, 9, https://doi.org/10.1186/s40645-024-00614-1, 2024.

Naegeli, K., Damm, A., Huss, M., Wulf, H., Schaepman, M., and Hoelzle, M.: Cross-Comparison of Albedo Products for Glacier Surfaces Derived from Airborne and Satellite (Sentinel-2 and Landsat 8) Optical Data, Remote Sensing, 9, 110, https://doi.org/10.3390/rs9020110, 2017.

Naegeli, K., Huss, M., and Hoelzle, M.: Change detection of bare-ice albedo in the Swiss Alps, The Cryosphere, 13, 397–412, https://doi.org/10.5194/tc-13-397-2019, 2019.

Ortiz Diaz, I., Lenzano, M. G., and Araneo, D.: Temporal Estimation of Snow Line Altitude in Glaciers of the Southern Patagonian Icefield Using Google Earth Engine, The International Archives of the Photogrammetry, Remote Sensing and Spatial Information Sciences, XLVIII-2/W6-2024, 19–24, https://doi.org/10.5194/isprs-archives-XLVIII-2-W6-2024-19-2024, 2024.

Otsu, N.: A threshold selection method from gray-level histograms, IEEE Transactions on Systems, Man, and Cybernetics, 9, 62–66, https://doi.org/10.1109/TSMC.1979.4310076, 1979.

Pandey, P., Kulkarni, A. V., and Venkataraman, G.: Remote sensing study of snowline altitude at the end of melting season, Chandra-Bhaga basin, Himachal Pradesh, 1980–2007, Geocarto International, 28, 311–322, https://doi.org/10.1080/10106049.2012.705336, 2013.

Paul, F., Frey, H., and Le Bris, R.: A new glacier inventory for the European Alps from Landsat TM scenes of 2003: challenges and results, Annals of Glaciology, 52, 144–152, https://doi.org/10.3189/172756411799096295, publisher: International Glaciological Society, 2011.

Paul, F., Winsvold, S., Kääb, A., Nagler, T., and Schwaizer, G.: Glacier Remote Sensing Using Sentinel-2. Part II: Mapping Glacier Extents and Surface Facies, and Comparison to Landsat 8, Remote Sensing, 8, 575, https://doi.org/10.3390/rs8070575, 2016.

Pepin, N. C., Arnone, E., Gobiet, A., Haslinger, K., Kotlarski, S., Notarnicola, C., Palazzi, E., Seibert, P., Serafin, S., Schöner, W., Terzago, S., Thornton, J. M., Vuille, M., and Adler, C.: Climate Changes and Their Elevational Patterns in the Mountains of the World, Reviews of Geophysics, 60, e2020RG000 730, https://doi.org/10.1029/2020RG000730, 2022.

Prieur, C., Rabatel, A., Thomas, J.-B., Farup, I., and Chanussot, J.: Machine Learning Approaches to Automatically Detect Glacier Snow Lines on Multi-Spectral Satellite Images, Remote Sensing, 14, 3868, https://doi.org/10.3390/rs14163868, 2022.

Puspitarini, H. D., François, B., Zaramella, M., Brown, C., and Borga, M.: The impact of glacier shrinkage on energy production from hydropower-solar complementarity in alpine river basins, Science of The Total Environment, 719, 137 488, https://doi.org/10.1016/j.scitotenv.2020.137488, 2020.

Rabatel, A., Dedieu, J.-P., and Vincent, C.: Using remote-sensing data to determine equilibrium-line altitude and mass-balance time series: validation on three French glaciers, 1994–2002, Journal of Glaciology, 51, 539–546, https://doi.org/10.3189/172756505781829106, 2005.

Racoviteanu, A. E., Rittger, K., and Armstrong, R.: An Automated Approach for Estimating Snowline Altitudes in the Karakoram and Eastern Himalaya From Remote Sensing, Frontiers in Earth Science, 7, 220, https://doi.org/10.3389/feart.2019.00220, 2019.

Rastner, P., Prinz, R., Notarnicola, C., Nicholson, L., Sailer, R., Schwaizer, G., and Paul, F.: On the Automated Mapping of Snow Cover on Glaciers and Calculation of Snow Line Altitudes from Multi-Temporal Landsat Data, Remote Sensing, 11, 1410, https://doi.org/10.3390/rs11121410, 2019.

Ren, S., Jia, L., Miles, E. S., Menenti, M., Kneib, M., Shaw, T. E., Buri, P., McCarthy, M. J., Yang, W., Pellicciotti, F., and Yao, T.: Observed and projected declines in glacier albedo across the Third Pole in the 21st century, One Earth, 7, 1587–1599, https://doi.org/10.1016/j.oneear.2024.08.010, 2024.

RGI-7.0-Consortium: Randolph Glacier Inventory - A Dataset of Global Glacier Outlines, Version 7.0, https://doi.org/https://doi.org/10.5067/f6jmovy5navz, 2023.

Rounce, D. R., Khurana, T., Short, M. B., Hock, R., Shean, D. E., and Brinkerhoff, D. J.: Quantifying parameter uncertainty in a large-scale glacier evolution model using Bayesian inference: application to High Mountain Asia, Journal of Glaciology, 66, 175–187, https://doi.org/10.1017/jog.2019.91, 2020.

Rounce, D. R., Hock, R., Maussion, F., Hugonnet, R., Kochtitzky, W., Huss, M., Berthier, E., Brinkerhoff, D., Compagno, L., Copland, L., Farinotti, D., Menounos, B., and McNabb, R. W.: Global glacier change in the 21st century: Every increase in temperature matters, Science, 379, 78–83, https://doi.org/10.1126/science.abo1324, 2023.

Salomonson, V. and Appel, I.: Estimating fractional snow cover from MODIS using the normalized difference snow index, Remote Sensing of Environment, 89, 351–360, https://doi.org/10.1016/j.rse.2003.10.016, 2004.

Schuster, L., Rounce, D. R., and Maussion, F.: Glacier projections sensitivity to temperature-index model choices and calibration strategies, Annals of Glaciology, 64, 293–308, https://doi.org/10.1017/aog.2023.57, 2023.

Shukla, A., Gupta, R., and Arora, M.: Estimation of debris cover and its temporal variation using optical satellite sensor data: a case study in Chenab basin, Himalaya, Journal of Glaciology, 55, 444–452, https://doi.org/10.3189/002214309788816632, 2009.

Sommer, C., Malz, P., Seehaus, T. C., Lippl, S., Zemp, M., and Braun, M. H.: Rapid glacier retreat and downwasting throughout the European Alps in the early 21st century, Nature Communications, 11, 3209, https://doi.org/10.1038/s41467-020-16818-0, 2020.

Sommer, C., Groos, A. R., Fürst, J., and Braun, M.: Transient snow line altitudes of glaciers in the European Alps from multi-mission remote sensing data (2000-2025), https://doi.org/10.5281/zenodo.18223929, 2026.

Spoto, F., Sy, O., Laberinti, P., Martimort, P., Fernandez, V., Colin, O., Hoersch, B., and Meygret, A.: Overview Of Sentinel-2, in: 2012 IEEE International Geoscience and Remote Sensing Symposium, pp. 1707–1710, IEEE, Munich, Germany, ISBN 978-1-4673-1159-5 978-1-4673-1160-1 978-1-4673-1158-8, https://doi.org/10.1109/IGARSS.2012.6351195, 2012.

Teillet, P., Barker, J., Markham, B., Irish, R., Fedosejevs, G., and Storey, J.: Radiometric cross-calibration of the Landsat-7 ETM+ and Landsat-5 TM sensors based on tandem data sets, Remote Sensing of Environment, 78, 39–54, https://doi.org/10.1016/S0034-4257(01)00248-6, 2001.

The GlaMBIE Team, Zemp, M., Jakob, L., Dussaillant, I., Nussbaumer, S. U., Gourmelen, N., Dubber, S., A, G., Abdullahi, S., Andreassen, L. M., Berthier, E., Bhattacharya, A., Blazquez, A., Boehm Vock, L. F., Bolch, T., Box, J., Braun, M. H., Brun, F., Cicero, E., Colgan, W., Eckert, N., Farinotti, D., Florentine, C., Floricioiu, D., Gardner, A., Harig, C., Hassan, J., Hugonnet, R., Huss, M., Jóhannesson, T., Liang, C.-C. A., Ke, C.-Q., Khan, S. A., King, O., Kneib, M., Krieger, L., Maussion, F., Mattea, E., McNabb, R., Menounos, B., Miles, E., Moholdt, G., Nilsson, J., Pálsson, F., Pfeffer, J., Piermattei, L., Plummer, S., Richter, A., Sasgen, I., Schuster, L., Seehaus, T., Shen, X., Sommer, C., Sutterley, T., Treichler, D., Velicogna, I., Wouters, B., Zekollari, H., and Zheng, W.: Community estimate of global glacier mass changes from 2000 to 2023, Nature, 639, 382–388, https://doi.org/10.1038/s41586-024-08545-z, 2025.

Thornton, J. M., Palazzi, E., Pepin, N. C., Cristofanelli, P., Essery, R., Kotlarski, S., Giuliani, G., Guigoz, Y., Kulonen, A., Pritchard, D., Li, X., Fowler, H. J., Randin, C. F., Shahgedanova, M., Steinbacher, M., Zebisch, M., and Adler, C.: Toward a definition of Essential Mountain Climate Variables, One Earth, 4, 805–827, https://doi.org/10.1016/j.oneear.2021.05.005, 2021.

Turpin, O., Ferguson, R., and Clark, C.: Remote sensing of snowline rise as an aid to testing and calibrating a glacier runoff model, Physics and Chemistry of the Earth, 22, 279–283, https://doi.org/10.1016/S0079-1946(97)00144-4, 1997.

USGS: Earth Resources Observation and Science (EROS) Center. Landsat 8-9 Operational Land Imager / Thermal Infrared Sensor Level-2, Collection 2 [dataset]., https://doi.org/https://doi.org/10.5066/P9OGBGM6., 2020.

Vermote, E. and Saleous, N.: LEDAPS surface reflectance product description, NASA, 2007.

Vermote, E., Roger, J., Franch, B., and Skakun, S.: LaSRC (Land Surface Reflectance Code): Overview, application and validation using MODIS, VIIRS, LANDSAT and Sentinel 2 data's, in: IGARSS 2018 - 2018 IEEE International Geoscience and Remote Sensing Symposium, pp. 8173–8176, IEEE, Valencia, ISBN 978-1-5386-7150-4, https://doi.org/10.1109/IGARSS.2018.8517622, 2018.

Warren, S. G.: Optical properties of ice and snow, Philosophical Transactions of the Royal Society A: Mathematical, Physical and Engineering Sciences, 377, 20180 161, https://doi.org/10.1098/rsta.2018.0161, publisher: The Royal Society, 2019.

WGMS: Fluctuations of Glaciers (FoG) Database, https://doi.org/https://doi.org/10.5904/wgms-fog-2025-02b, 2025.

Williams, R. S., Hall, D. K., and Benson, C. S.: Analysis of glacier facies using satellite techniques, Journal of Glaciology, 37, 120–128, https://doi.org/10.3189/S0022143000042878, 1991.

Wulder, M. A., Roy, D. P., Radeloff, V. C., Loveland, T. R., Anderson, M. C., Johnson, D. M., Healey, S., Zhu, Z., Scambos, T. A., Pahlevan, N., Hansen, M., Gorelick, N., Crawford, C. J., Masek, J. G., Hermosilla, T., White, J. C., Belward, A. S., Schaaf, C., Woodcock, C. E., Huntington, J. L., Lymburner, L., Hostert, P., Gao, F., Lyapustin, A., Pekel, J.-F., Strobl, P., and Cook, B. D.: Fifty years of Landsat science and impacts, 280, 113 195, https://doi.org/10.1016/j.rse.2022.113195, 2022.

Xie, F., Liu, S., Zhu, Y., Qing, X., Tan, S., Gao, Y., Qi, M., Yi, Y., Ye, H., Afzal, M. M., Zhang, X., and Zhou, J.: Retrieval of high-resolution melting-season albedo and its implications for the Karakoram Anomaly, Remote Sensing of Environment, 315, 114 438, https://doi.org/10.1016/j.rse.2024.114438, 2024.

Yin, D., Cao, X., Chen, X., Shao, Y., and Chen, J.: Comparison of automatic thresholding methods for snow-cover mapping using Landsat TM imagery, International Journal of Remote Sensing, 34, 6529–6538, https://doi.org/10.1080/01431161.2013.803631, 2013.

Zhang, H. and Roy, D.: Computationally Inexpensive Landsat 8 Operational Land Imager (OLI) Pansharpening, Remote Sensing, 8, 180, https://doi.org/10.3390/rs8030180, 2016.

Zhang, Q. and Kang, S.: Glacier snowline altitude variations in the Pamirs, Tajikistan, 1998-2013: insights from remote sensing images, Remote Sensing Letters, 8, 1220–1229, https://doi.org/10.1080/2150704X.2017.1375611, 2017.

Østrem, G.: Erts Data in Glaciology—An Effort to Monitor Glacier Mass Balance from Satellite Imagery, Journal of Glaciology, 15, 403–415, https://doi.org/10.3189/S0022143000034511, 1975.